Chemical Science

EDGE ARTICLE

View Article Online
View Journal | View Issue

Cite this: *Chem. Sci.*, 2014, **5**, 1187

Electronic and molecular structures of the active-site H-cluster in [FeFe]-hydrogenase determined by site-selective X-ray spectroscopy and quantum chemical calculations†

Camilla Lambertz,‡[a] Petko Chernev,[b] Katharina Klingan,[b] Nils Leidel,[b] Kajsa G. V. Sigfridsson,§[b] Thomas Happe[a] and Michael Haumann*[b]

The [FeFe]-hydrogenase (HydA1) from green algae is the minimal enzyme for efficient biological hydrogen (H_2) production. Its active-site six-iron center (H-cluster) consists of a cubane, $[4Fe4S]_H$, cysteine-linked to a diiron site, $[2Fe]_H$. We utilized the spin-polarization of the iron Kβ X-ray fluorescence emission to perform site-selective X-ray absorption experiments for spectral discrimination of the two sub-complexes. For the H-cluster in reduced HydA1 protein, XANES and EXAFS spectra, Kβ emission lines (3p → 1s transitions), and core-to-valence (pre-edge) absorption (1s → 3d) and valence-to-core ($K\beta^{2,5}$) emission (3d → 1s) spectra were obtained, individually for $[4Fe4S]_H$ and $[2Fe]_H$. Iron–ligand bond lengths and intermetal distances in $[2Fe]_H$ and $[4Fe4S]_H$ were resolved, as well as fine structure in the high-spin iron containing cubane. Density functional theory calculations reproduced the X-ray spectral features and assigned the molecular orbital configurations, emphasizing the asymmetric d-level degeneracy of the proximal (Fe_p) and distal (Fe_d) low-spin irons in $[2Fe]_H$ in the non-paramagnetic state. This yielded a specific model structure of the H-cluster with a bridging carbon monoxide ligand and an apical open coordination site at Fe_d in $[2Fe]_H$. The small HOMO–LUMO gap (~0.3 eV) enables oxidation and reduction of the active site at similar potentials for reversible H_2 turnover by HydA1, the LUMO spread over $[4Fe4S]_H$ supports its role as an electron transfer relay, and Fe_d carrying the HOMO is prepared for transient hydride binding. These features and the accessibility of Fe_d from the bulk phase can account for regio-specific redox transitions as well as H_2-formation and O_2-inhibition at the H-cluster. We provide a conceptual and experimental framework for site-selective studies on catalytic mechanisms in inhomogeneous materials.

Received 26th September 2013
Accepted 19th November 2013

DOI: 10.1039/c3sc52703d

www.rsc.org/chemicalscience

Introduction

Hydrogen (H_2) is an outstandingly attractive renewable fuel resource for energy supply in the future.[1,2] However, at present the cost-efficient production of H_2 is limited for example by the need for precious catalyst materials such as platinum.[3,4] Research efforts thus focus on the development of novel H_2-forming catalysts, which are based on abundant and inexpensive transition metals.[5–8] Iron is particularly appealing,[8–11] but Fe-systems, showing H_2-production rates and turnover numbers sufficiently high for applications, so far are not available.[12]

Nature provides efficient H_2-forming catalysts in form of [FeFe]-hydrogenase proteins.[13–15] These enzymes are the most active biological H_2 producers from proton reduction with turnover rates up to 10^4 s^{-1}.[13,16] However, a limitation for technological application is enzyme inactivation by dioxygen (O_2).[17–19] The [FeFe]-hydrogenase (HydA1) from the green alga *Chlamydomonas reinhardtii* is the minimal unit of biological H_2-formation,[13] because it binds only the active site of

[a]*Institute for Biochemistry of Plants, Department of Photobiotechnology, Ruhr-University Bochum, 44780 Bochum, Germany*

[b]*Institute for Experimental Physics, Freie Universität Berlin, FB Physik, Arnimallee 14, 14195 Berlin, Germany. E-mail: michael.haumann@fu-berlin.de; Fax: +49 30 838 56299; Tel: +49 30 838 56101*

† Electronic supplementary information (ESI) available: Details on protein sample preparation procedures; spin- and site-selective XAE on a Fe_2O_3 and $Fe_2(CO)_9$ powder mixture (Fig. S1), Kβ emission spectra of iron reference compounds (Fig. S2), XANES spectra of proteins and reference compounds (Fig. S3), EXAFS spectra of proteins and reference compounds (Fig. S4), valence-to-core emission spectra for HydA1(apo) and FDX(4Fe) (Fig. S5), site-selective pre-edge absorption spectra for HydA1(rai) (Fig. S6), structures and XAE spectra for alternative spin configurations (Fig. S7), comparison of unprotonated and protonated H-cluster structures (Fig. S8), the H-cluster model in the HydA1 crystal structure (Fig. S9), EXAFS simulation parameters for reference compounds (Table S1), coordinates of the H-cluster model structure in Fig. 6 (Table S2), supporting references. See DOI: 10.1039/c3sc52703d

‡ Present address: Molecular Biotechnology, RWTH Aachen, 52074 Aachen, Germany.

§ Present address: MAX IV Laboratory, Lund University, 22100 Lund, Sweden.

H_2-production, which is a six-iron complex denoted H-cluster.[20,21] Further iron–sulfur clusters as found in bacterial [FeFe]-hydrogenases are absent. HydA1 thus represents an ideal model system for spectroscopy to focus on the active site structure and the O_2-inhibition and H_2-formation reactions.[22–24]

The general organization of the H-cluster has been revealed by crystallography on bacterial enzymes (Fig. 1).[25–27] It features a cubane-type iron–sulfur cluster, $[4Fe4S]_H$, which is bound by four cysteine residues to the protein and is linked by one of them to a binuclear iron unit, $[2Fe]_H$. The Fe ions of $[2Fe]_H$ in proximal or distal positions relative to $[4Fe4S]_H$ are denoted Fe_p and Fe_d. This structure is assembled with the aid of three maturation proteins.[28,29] For HydA1, a crystal structure only of the apo-protein was reported, which contains $[4Fe4S]_H$, but lacks the $[2Fe]_H$ unit.[30] The structures of the mature H-cluster in some aspects are ambiguous, for example with respect to the nature and positioning of the diatomic ligands, open coordination sites at the diiron unit, and the metal bridging entity in $[2Fe]_H$ (Fig. 1). The varying features partly were attributed to different functional states of the site,[26] but may as well reflect resolution limitations due to redox state heterogeneity in the crystals, influencing ligand orientations[24,31] and metal–metal distances.[22,32]

Infrared spectroscopy (FTIR) has facilitated assignment of the diatomic ligands as two cyanide (CN^-) and three carbon monoxide (CO) molecules[24,31,33,34] and these ligands were also detected by nuclear resonance methods.[35] In FTIR and EPR studies, several redox states of the H-cluster have been assigned.[31,36,37] Advanced magnetic resonance techniques have favored attribution of the metal bridge in $[2Fe]_H$ to an azadithiolate group (adt, $(SCH_2)_2NH$).[37] This suggestion recently has been proven by functional reconstitution of apo-HydA1 only with a synthetic $[2Fe]_H$ analogue, which contained an adt bridge.[38,39] Electronic features for paramagnetic redox states of the H-cluster were revealed by EPR[24,36] and Mössbauer spectroscopy.[40] These results have greatly advanced our understanding of the site architecture and function. However, the used techniques do not directly deduce the molecular structure, defined by the interatomic distances, and its relation to the electronic properties, *i.e.* molecular orbital (MO) configurations, in particular for non-paramagnetic states of the center.

The $[2Fe]_H$ unit is believed to be the actual active site of the H_2 chemistry[41–44] and also to be the primary target of O_2 attack during inhibition.[17–19,45,46] Hydride (H^-) binding to $[2Fe]_H$, for example in the super-reduced state, has been proposed.[24,47,48] We and others have suggested the bonding of reactive oxygen species (ROS) to $[2Fe]_H$.[17–19,45,46] The locations and mechanisms of both the H_2-formation and O_2-inhibition reactions, however, remain insufficiently understood on the molecular level, at least from an experimental point of view. Deeper insight is expected

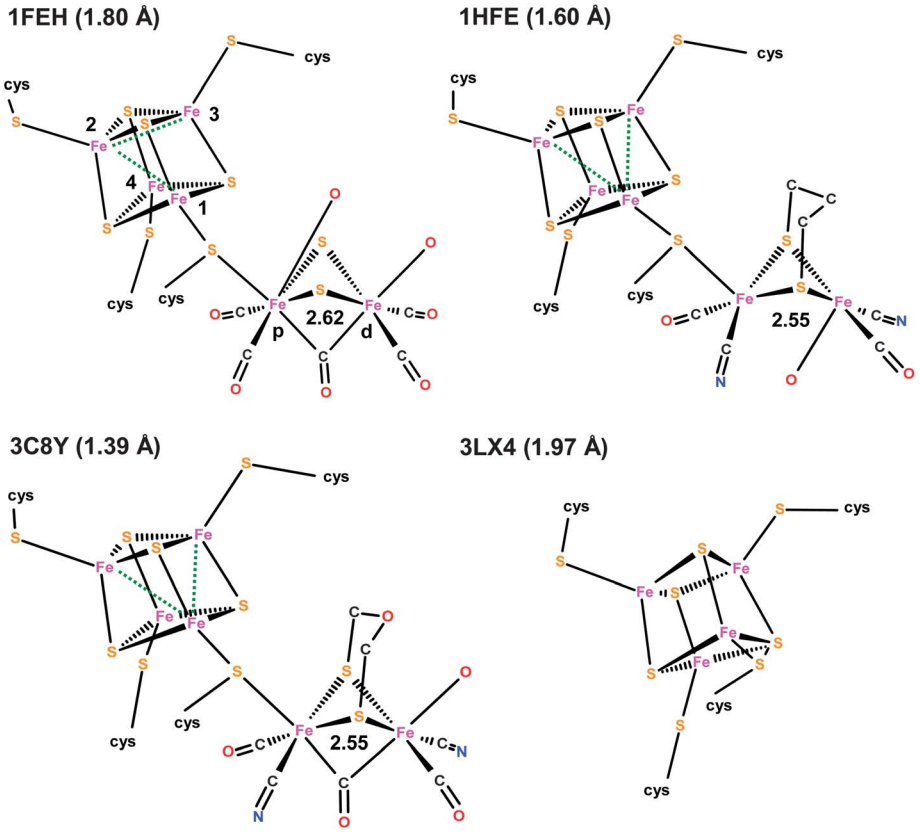

Fig. 1 Crystallographic structures of the H-cluster. Indicated PDB entry codes (resolution in parenthesis) correspond to the following [FeFe]-hydrogenases and organisms: 1FEH and 3C8Y, CpI from *Clostridium pasteurianum*; 1HFE, DdH from *Desulfovibrio desulfuricans*; 3LX4, HydA1 apo-enzyme from *Chlamydomonas reinhardtii*. Fe–Fe distances in Å, green dotted lines mark long Fe–Fe distances in $[4Fe4S]_H$, cys denotes cysteine residues; p and d denote the proximal and distal irons of $[2Fe]_H$ and numbers 1–4 the iron atoms in $[4Fe4S]_H$.

from determination of the regio-selectivity of hydride and ROS bonding at the H-cluster using novel experimental approaches.

Synthetic chemistry has produced a wealth of molecular model complexes, which reproduce essential structural features of $[2Fe]_H$ (see for example ref. 8, 12, 20 and 49–53). However, the diiron systems usually show low H_2 turnover rates. This reflects (i) the formation of thermodynamically trapped Fe–Fe bridging hydride species,[52,54–58] (ii) low efficiencies of electron donation to the complexes, highlighted by activity enhancement for molecular catalysts immobilized on conductive materials,[6,59] and (iii) restraints in proton funneling to the active site, emphasized by the boosting effect of pendant bases next to the metal centers.[7,60] At the H-cluster, the proton and electron management may be optimized by terminal hydride binding to $[2Fe]_H$, functioning of $[4Fe4S]_H$ as an electron transfer relay, and an amine base in the adt bridge. These suggestions need to be proven, thus calling for experimental techniques to monitor ligation changes and redox reactions selectively at the $[2Fe]_H$ and $[4Fe4S]_H$ units.

High-resolution X-ray absorption spectroscopy (XAS) in combination with narrow-band X-ray fluorescence detection (XES) is facilitated by strong undulator beamlines at 3rd-generation synchrotrons.[61–63] This approach (XAE) provides simultaneous access to structural features (precise bond lengths, metal–metal distances, site geometries)[64,65] and electronic properties (oxidation state; configuration, energy and occupancy of valence MOs).[66,67] The intrinsic spin-polarization of the underlying electronic excitation and decay transitions allows discrimination of high- and low-spin and differently coordinated metal sites in heterogeneous samples.[68–71] This site-selectivity is based, *e.g.*, on the collection of XAS spectra for varying emission energies, at which one or the other metal species predominantly contributes. By XAE, individual structural parameters for asymmetric Fe ions were determined and hydride species were detected in diiron complexes.[72–74] The particular sensitivity of the Kβ emission for protein studies, owing to strong electronic interactions between metal-3p and valence electrons, was demonstrated recently.[75,76] However, determination of sub-structures in a complex protein-bound metal center by XAE has not been attempted so far.

Here, we utilized the spin-selectivity of the Fe Kβ emission to access the individual molecular and electronic structures of $[2Fe]_H$ and $[4Fe4S]_H$ in a reduced state of the H-cluster in HydA1 by a site-selective approach. XANES and EXAFS spectra, Kβ emission (3p → 1s), core-to-valence (pre-edge) absorption (1s → 3d), and valence-to-core (Kβ^{2,5}) emission (3d → 1s) spectra were obtained for both units. The underlying electronic transitions were assigned by DFT calculations. This yielded a model structure of the H-cluster, which accounts for the regio-specific redox reactions and chemistry at the active site.

Materials and methods

Protein sample preparation

C. reinhardtii [FeFe]-hydrogenase, HydA1(rai), was overexpressed heterologously in *Clostridium acetobutylicum* (strain ATCC 824), purified *via* Strep-Tag affinity chromatography with O_2-free buffer (100 mM Tris/HCl (pH 8.0), 2 mM sodium dithionite (NaDT)), and stored at −80 °C in the same buffer supplemented with 10% (v/v) glycerol until use, as previously described.[22,77] For further details of sample preparation see the ESI.† The apo-protein of the [FeFe]-hydrogenase, HydA1(apo), containing only the $[4Fe4S]_H$ unit, was obtained by protein overexpression in *E. coli* strain BL21 DE3 DiscR using a pET plasmid lacking the respective maturases (HydE, HydG, HydF) for assembling the active H-cluster structure.[38,78] Clostridial ferredoxin, FDX(4Fe), was overexpressed in *C. acetobutylicum* and purified as described elsewhere.[79] Enzyme purification and concentration to up to 2 mM (Amicon Ultracel 10 kDa, Millipore) were performed under strictly anaerobic conditions in an anaerobic tent. Aliquots of protein samples (20 μl) were transferred into Kapton-covered acrylic-glass sample holders for XAE and stored in liquid N_2 until use.

X-Ray spectroscopy

X-Ray absorption and emission spectroscopy was carried out at the undulator beamline ID26 of the European Synchrotron Radiation Facility (ESRF) at Grenoble (France) as previously described.[72–74] Samples were held in a laboratory-built liquid-He cryostat at 20 K. The incident energy was set by an Si[311] double-crystal monochromator (energy bandwidth ∼0.2 eV at the Fe K-edge). Conventional Kα-detected XAS spectra were collected using a scintillation detector[80] (∼20 cm^2 area, placed at 90° to the incident X-ray beam and at ∼1 m to the sample), which was shielded by 10 μm Mn foil against scattered incident X-rays. EXAFS oscillations were extracted from XAS data as described before[81] (E_0 of 7112 eV) and unfiltered k^3-weighted EXAFS spectra were used for least-squares multiple-scattering curve-fitting and Fourier-transform (FT) calculation using in-house software.[81] EXAFS phase-functions were calculated with FEFF8 (group of J. J. Rehr, University of Washington[82]). E_0 was refined to ∼7120 eV in the EXAFS fits (S_0^2 of 0.85). High energy-resolution emission detection (energy bandwidths ∼1.3 eV or ∼1.0 eV at the Fe Kα or Kβ fluorescence lines) was achieved by using a vertical-plane Rowland-circle spectrometer, equipped with five spherically-bent Ge wafers (R = 1000 mm; Ge[440], Kα or Ge[620], Kβ) for fluorescence monochromatization, and a silicon-drift detector or an avalanche photodiode (APD) for monitoring of the X-ray fluorescence. The incident and emission energy axes of the spectrometer were calibrated (accuracy ±0.1 eV) using the absorption of an Fe foil (reference energy of 7112 eV) and the elastic scattering peak. XAS spectra at the Fe K-edge were measured using the rapid-scan mode of ID26 (total scan durations of 1–5 s for XANES spectra and 20–30 s for EXAFS spectra; 0.2–0.3 eV per step) and simultaneous scanning of the monochromator and of the gaps of the three undulators of the beamline. For collection of RIXS plane data, the emission detection energy was varied over the Kβ spectral region in 0.3–0.4 eV steps; RIXS data were averaged and evaluated using in-house Matlab (Mathsoft) tools. The pre-edge region of XANES spectra was isolated using the program XANDA.[83] The absence of radiation damage in the protein samples was assured by limiting the X-ray irradiation by frequent sample spot changes and use of a rapid beamshutter during spectrometer

movements, and verified by comparison of Kα-detected XANES spectra prior to and after the XAE experiments, which were identical within resolution limits (not shown). For a schematic depiction of the experimental set-up for XAE see ref. 72.

Density functional theory calculations

Geometry-optimization of H-cluster model structures and spin-unrestricted single-point calculations were performed with the DFT program package ORCA.[84] The BP86 exchange correlation functional[85–87] and a triple-zeta valence plus double polarization (TZVPP) basis set[88] were used, as previously.[72–74] The COSMO solvation model[89] with a dielectric constant of $\varepsilon = 4$ was used in the geometry optimizations. DFT calculations were based on a model structure, which was constructed using crystallographic data for the bacterial H-cluster,[90] and comprised a singlet ground state, a spin multiplicity of $M = 1$, and. a total charge of −4. The cysteine side chains of the thiol ligands to $[4Fe4S]_H$ were truncated to S–CH_3 groups and in the geometry optimizations, the carbon atoms of the four S–CH_3-groups were fixed at their crystallographic positions. A broken-symmetry approach[91] was used as implemented in ORCA.[92] by first calculating the high-spin configuration, then the spin directions on two iron atoms in $[4Fe4S]_H$ and on Fe_p in $[2Fe]_H$ of the H-cluster were inverted, and finally the system was converged to the antiferromagnetic configuration. For further details see the Results. The resulting MOs were visualized as isosurfaces with the programs Jmol or UCSF Chimera. X-Ray absorption K-edge intensities in the pre-edge region (core-to-valence transitions) were calculated using a time-dependent DFT formalism[73,93] and Kβ valence-to-core transitions ($K\beta^{2,5}$ emission) were calculated using the DFT approach described in ref. 72 and 78 (see also ref. 72–74). A shift to higher energies by 181 eV and Gaussian broadening of stick spectra (see figure legends) were applied to calculated Kβ emission lines and pre-edge absorption spectra for comparison with the experimental data. The energy shift compensated for an underestimation of the calculated transition energies on the order of 2–3% compared to the experiment due to limitations of DFT in modeling the potentials near the nucleus, which results in an Fe 1s orbital that is slightly too high in energy relative to the valence orbitals, yielding the same systematic energy deviation for all complexes calculated with the same functional/basis set combination; energy shifts of similar magnitude have been applied by us and other authors in previous investigations.[72–75,94–96]

Results

Principles and methods for spin- and site-selective XAE

Theoretical background and spectra observed. Combined high-resolution X-ray absorption (XAS) and narrow-band detection emission (XES) spectroscopy experiments (XAE) were carried out to employ the intrinsic site- and spin-selectivity for discrimination of individual iron sites in the H-cluster. The principles of XAE in an atomistic picture are outlined in Fig. 2. Excitation of a core-level electron (1s) of iron for increasing energy leads (1) to resonant transitions into unoccupied valence states (with, *e.g.*, Fe 3d character), giving rise to the pre-edge absorption feature, (2) to transitions into virtual bound unoccupied levels (with, *e.g.*, Fe 4p character), causing the K-edge (XANES) absorption spectrum, and (3) to non-resonant transitions into the continuum, for which modulation of the absorption (EXAFS oscillations) occurs due to interference of the outgoing and backscattered (at the metal ligands) photoelectron waves. The core-to-valence (pre-edge) absorption (1s → 3d) thus probes the energies and configurations of unoccupied valence states. Electronic decay into the core hole with decreasing probability thereafter occurs from the 2p, 3p, and valence (with, *e.g.*, Fe 3d character) levels and gives rise to the $K\alpha^{1,2}$, Kβ and $K\beta^{2,5}$ emission lines, showing decreasing relative intensities of about 10 : 1 : 0.1. The valence-to-core ($K\beta^{2,5}$) emission (*e.g.* 3d → 1s) thus probes the energies and configurations of occupied valence states.

A splitting of the Kβ emission (3p → 1s) into the more intense $K\beta^{1,3}$ and weaker Kβ′ features results from coupling between the spin-up (α) (or spin-down, β) decaying 3p-electron and unpaired α (or β) 3d electrons (Fig. 2) so that the intensity of the Kβ′ relative to the $K\beta^{1,3}$ intensity increases for an increasing number of unpaired 3d spins.[71,72,97] For non-resonant excitation, promotion of both α and β 1s-electrons into the continuum can occur and the intensity of the Kβ′ emission is large for example for high-spin (hs) d^6 Fe(II) or d^5 Fe(III) species with four or five unpaired 3d α-spins and small for example for low-spin (ls) d^6 Fe(II) species with zero unpaired 3d spins. Notably, for ls diiron–carbonyl complexes with formal d^7 Fe(I) states, the surplus d-electrons usually pair, so that the Kβ′ emission is similarly small as that of ls d^6 Fe(II) compounds.[72–74] In the case of resonant excitation (1s → 3d), for hs Fe(II) or Fe(III) only excitation and decay of α-spin electrons can occur so that in the absence of coupling between unpaired α-spin and the decaying β-spin, the Kβ′ intensity is negligibly small. For ls Fe(II) (and Fe(I) in diiron compounds, see above), excitation of both α- and β-electrons is feasible and results in a surplus unpaired 3d spin, so that excitation and decay of electrons with the same spin flavour can occur, which increases the Kβ′ intensity (Fig. 2).

The above reasoning and the strict localization of the 3p orbitals at each iron atom imply that site-selectivity in XAS spectra, meaning discrimination of, *e.g.*, hs Fe(II)/(III) and ls Fe(I)/(II) species in a single sample, is obtained by exploitation of the spin-selectivity of the Kβ′ and $K\beta^{1,3}$ emission lines. For a mixture of hs and ls iron sites, non-resonant XAS spectra (XANES, EXAFS) should reflect for Kβ′-detection mainly the hs sites and for $K\beta^{1,3}$ detection mainly the ls sites. However, multiplet structure in the Kβ′ and $K\beta^{1,3}$ spectra, for example due to d-level energy splitting, and variations in the Kβ emission energy, due to different iron oxidation states and ligand species, may cause a more sophisticated distribution of site contributions to the XAS spectra as function of the Kβ-detection energy. For resonant excitation (pre-edge), the Kβ′-detected spectrum should be dominated by ls species and the $K\beta^{1,3}$-detected spectrum by hs species. Site-selectivity in Kβ emission spectra is obtained for resonant excitation into valence levels of the individual iron species. However, site-selectivity in the $K\beta^{2,5}$ (valence-to-core) emission may be flawed for extended

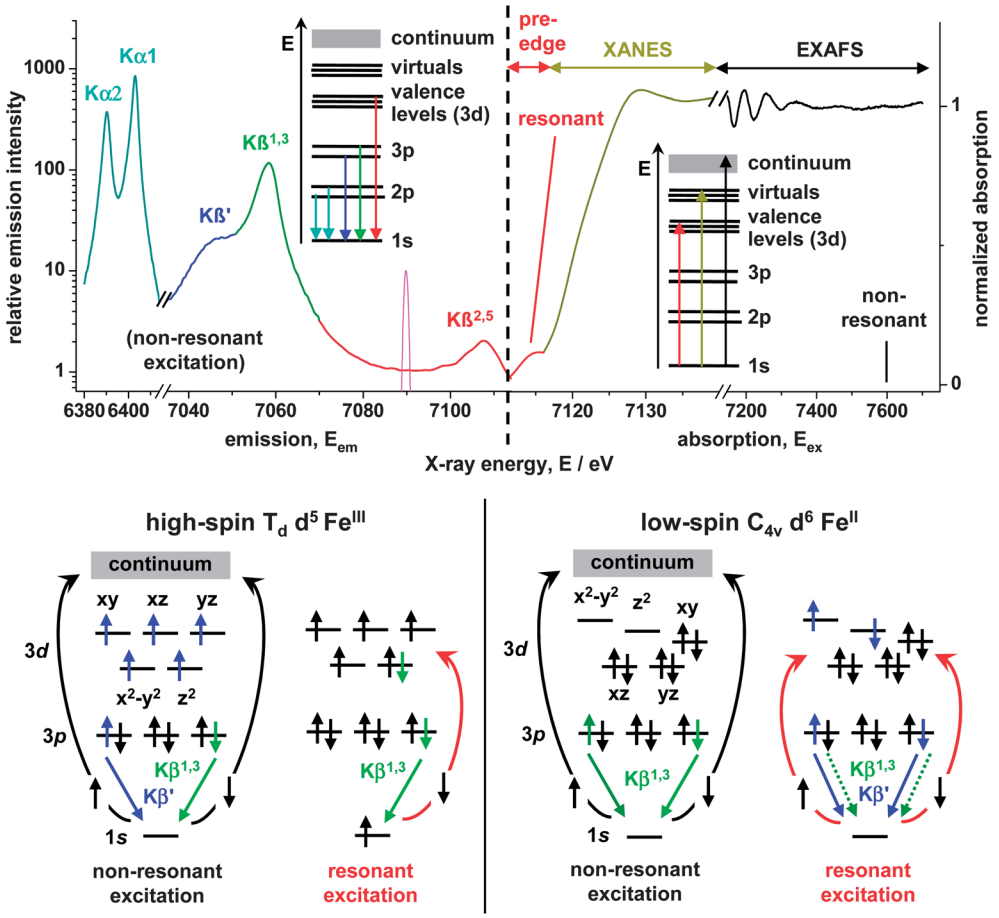

Fig. 2 Outline of spin- and site-selectivity in XAE spectroscopy. (Top) X-ray absorption (right) and emission (left; note the logarithmic *y*-axis) spectra of iron in [FeFe]-hydrogenase HydA1 on a common energy scale. The insets exemplify the electronic transitions in an atomic level picture, which correspond to the absorption and emission spectra. The magenta peak shows the Kβ detection energy resolution of ~1 eV. (Bottom) electronic transitions for non-resonant and resonant excitation of hs Fe(III) (left) and ls Fe(II) (right) species in similar coordination geometries as in the H-cluster. Coupling between unpaired valence level (Fe 3d) spins and the spin of the decaying 3p electron with the same flavour leads to a splitting of the 3p energy levels and thus of the Kβ emission line, increasing the Kβ′ intensity. In the absence of such spin–spin interactions mainly $K\beta^{1,3}$ emission is observed. This causes for non-resonant excitation dominance of hs iron in the Kβ′ region and for resonant excitation dominance of ls iron in the Kβ′ region (the green dotted lines denote $K\beta^{1,3}$ intensity due to multiplet structure), so that site-selectivity in XAS *via* the XES spin-selectivity is obtained.

structures by delocalization of valence MOs with mixed metal and ligand characters.

Verification of site-selectivity in XAE for a reference system. The above principles first were verified by XAE experiments on a powder mixture of $Fe^{III}{}_2O_3$ oxide (hematite) containing hs $Fe^{III}O_6$ sites and $Fe_2(CO)_9$ containing ls $Fe^0(CO)_6$ sites (Fig. S1†). These compounds were chosen because the spin and oxidation states, iron coordination by (CO)-ligands, and the stoichiometry of 70% hs to 30% ls sites in the mixture to a reasonable extent resembled the expected properties in the H-cluster. The Kα-emission detected XANES spectra and the Kβ and $K\beta^{2,5}$ emission lines for non-resonant excitation of the mixture represented stoichiometrically weighted sums of the spectra of the individual compounds. For non-resonant excitation, the Kβ′-emission (at ~7045 eV) was dominated to ~80% by the hs sites (enrichment factor of ~1.1 compared to the stoichiometry in the mixture); the maximal hs contribution to the $K\beta^{1,3}$ emission (at ~7061 eV) was ~90% (enrichment ~1.3). The maximal ls site contribution (at ~7057 eV) was ~57% (enrichment ~1.9).

From linear combinations (i) of EXAFS spectra detected at selected Kβ′- or $K\beta^{1,3}$-emission energies of the mixture with Kα-detected spectra of the pure compounds or of the mixture or (ii) of the Kβ′- and $K\beta^{1,3}$-detected EXAFS spectra, employing scaling factors as derived from the site stoichiometry and the energy-dependent relative contributions of the two species to the spectra, deconvoluted EXAFS spectra were obtained from the mixture, which closely matched the spectra of the pure compounds (Fig. S1†). This was confirmed by EXAFS simulations reproducing the Fe-ligand bond lengths and Fe–Fe distances in the crystal structures (Table S1†). For resonant excitation (pre-edge), the ls sites contributed ~85% to the Kβ′-emission (enrichment ~2.8) and the hs sites contributed maximally ~70% to the $K\beta^{1,3}$ emission and the respective core-to-valence (pre-edge) spectra of the mixture thus were similar to

the pure compounds (Fig. S1†). These results implied that adequate selection of excitation and Kβ emission energies and weighted combination of Kβ- and Kα-detected spectra can provide clean XAS and XES spectra of the different iron species in the H-cluster.

XAE on the H-cluster of [FeFe]-hydrogenase

Selection of model compounds for the H-cluster sub-complexes. For the H-cluster of HydA1, the energy-dependent relative contributions of $[2Fe]_H$ and $[4Fe4S]_H$ to the Kβ-emission spectrum *a priori* were unknown, complicating the derivation of pure XAS and XES spectra. Therefore, we studied the dependence of the Kβ emission spectrum on the ligand environment for several reference compounds (Fig. S2†). The Kβ spectrum of a synthetic diiron complex, PDT(2Fe) = (μ-pdt)$[Fe(CO)_2(PMe_3)]_2$ (pdt = $SC1H_2C2H_2C3H_2S$),[74,98] containing two ls formal Fe(I) ions with each 2 S, 2 (CO) and 1 PMe_3 in the ligand sphere, was well reproduced by summation of the weighted Kβ spectra of $Fe^0{}_2(CO)_9$ (× 0.4), $Fe^{II}(CN)_6$ (× 0.2) and $Fe^{II}S_2$ (× 0.4) (Fig. S2-A†). This showed that the Kβ emission in good approximation can be considered as a stoichiometric combination of spectra of Fe ions with only a single ligand species. In addition, the Kβ spectra for phosphine (PMe_3) and (CN) ligands are similar. Accordingly, we choose PDT(2Fe) as a suitable model for $[2Fe]_H$. Purified ferredoxin protein, FDX(4Fe), from *C. acetobutylicum* with two [4Fe4S] clusters[79] and HydA1 apo-protein, HydA1(apo), containing only the cubane cluster (Fig. 1), served as references for $[4Fe4S]_H$.

Kβ spectra for non-resonant excitation. The Kβ spectra for non-resonant excitation of HydA1(apo) and FDX(4Fe) were rather similar and typical for hs Fe(II) or Fe(III) species in showing pronounced Kβ′ emission intensities. The $Kβ^{1,3}$ maximum was at ~0.3 eV higher energy for HydA1(apo) (Fig. 3A). For ls sulfur-coordinated and for hs oxygen-coordinated Fe(II) and Fe(III) species, an up-shift of the $Kβ^{1,3}$ energy by ~0.9 eV was observed (Fig. S2-B†). This suggested that at least one iron atom per [4Fe4S] cluster was by one unit more oxidized in HydA1(apo) compared to FDX(4Fe). The spectrum of PDT(2Fe) revealed the ls character by the low Kβ′ intensity and the $Kβ^{1,3}$ maximum was at lower energy compared to HydA1(apo), reflecting the influence of the (CO) and PMe_3 ligands and the low iron oxidation state. The ratio of the Kβ spectra of PDT(2Fe) and HydA1(apo) was calculated, after 2 : 4 scaling of the spectra using the stoichiometry of iron atoms in the two H-cluster sub-units, yielding the relative contributions of the two species as function of the Kβ emission energy (Fig. 3A, inset). This showed that the Kβ′ (~7045 eV) and high-energy $Kβ^{1,3}$ emission (~7060 eV) were highly selective (~78% and ~75%, enrichment ~1.2) for $[4Fe4S]_H$. The maximal selectivity for $[2Fe]_H$ in the $Kβ^{1,3}$ emission (~7057 eV) was close to 50% (enrichment ~1.5).

The non-resonant Kβ spectrum for HydA1(rai) was intermediate between PDT(2Fe) and FDX(4Fe) or HydA1(apo) regarding its Kβ′ intensity and $Kβ^{1,3}$ energy; the shape reflected the dominance of $[4Fe4S]_H$ (Fig. 3A). Subtraction of the stoichiometrically scaled HydA1(apo) spectrum from the HydA1(rai) spectrum yielded a spectrum, which was almost identical to PDT(2Fe). We consider the respective spectra within resolution and noise limits as being identical to the non-resonant Kβ

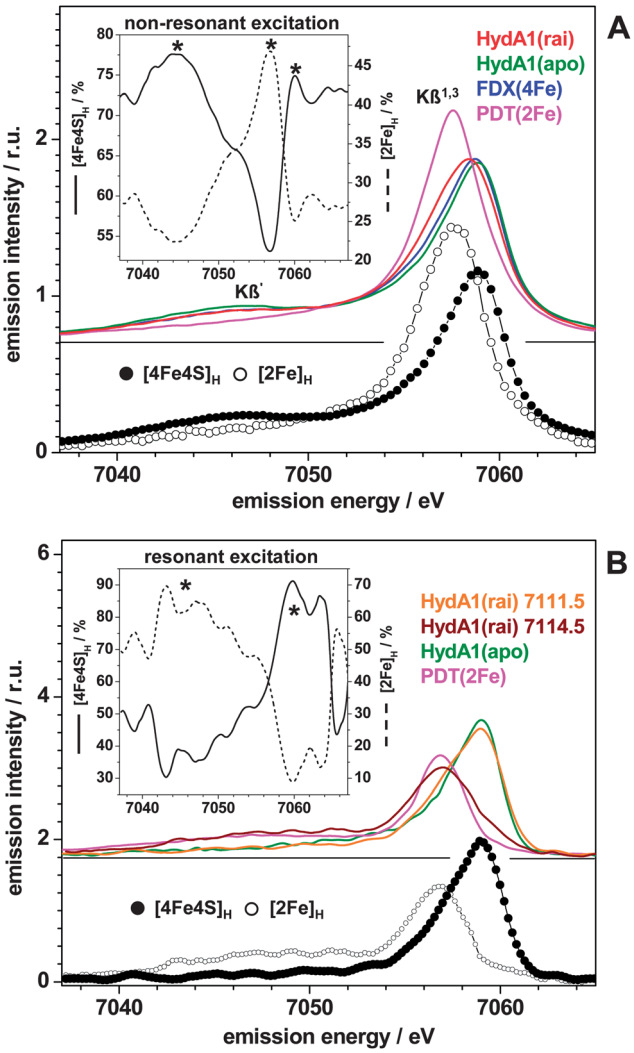

Fig. 3 Kβ emission spectra (3p → 1s) of HydA1. Spectra in (A) and (B) were normalized to unity areas under the curves. (A) Kβ spectra for non-resonant excitation (7600 eV). Top: HydA1(rai), reduced as-isolated [FeFe]-hydrogenase from *C. reinhardtii* containing the H-cluster; HydA1(apo), apo-enzyme containing only $[4Fe4S]_H$; FDX(4Fe), ferredoxin from *C. acetobutylicum* with two [4Fe4S] clusters; PDT(2Fe), synthetic diiron complex, (μ-pdt)$[Fe(CO)_2(PMe_3)]_2$ (pdt = $SC1H_2C2H_2C3H_2S$), which is a model for $[2Fe]_H$ (Fig. S2†). Bottom: spectra corresponding to $[4Fe4S]_H$, *i.e.* to the HydA1(apo) spectrum, and $[2Fe]_H$, from calculation of the difference of stoichiometrically weighted spectra and re-normalization ($[2Fe]_H$ = (HydA1(rai) × 6 − HydA1(apo) × 4) × 0.5). Inset: relative contributions of $[4Fe4S]_H$ and $[2Fe]_H$ to the HydA1 Kβ spectrum ($[4Fe4S]_H$) = $[4Fe4S]_H$ × 4/($[4Fe4S]_H$ × 4 + $[2Fe]_H$ × 2) and *vice versa* for $[2Fe]_H$). (B) Kβ spectra for resonant excitation (top) into the pre-edge absorption feature (Fig. 4 and S3†) for HydA1(rai) at the indicated energies, for HydA1(apo) at 7113.0 eV, and for PDT(2Fe) at 7113.5 eV. Bottom spectra: $[4Fe4S]_H$ = $(HydA1(rai)_{7111.5}$ − $HydA1(rai)_{7114.5}$ × 0.1) × 1.11 and $[2Fe]_H$ = $(HydA1(rai)_{7114.5}$ − $HydA1(rai)_{7111.5}$ × 0.2) × 1.25. Inset: estimated relative contributions of $[4Fe4S]_H$ and $[2Fe]_H$ derived as outlined under (A). Asterisks mark Kβ emission energies, at which highest selectivity for the two sub-complexes of the H-cluster is observed. Spectra were vertically displaced for comparison.

spectra of the $[2Fe]_H$ and $[4Fe4S]_H$ units of the H-cluster (Fig. 3A). The $[2Fe]_H$ Kβ spectrum revealed the ls character of the two iron atoms by the small Kβ′ intensity and the (CO/N) Fe-coordination by the low-energy $K\beta^{1,3}$ maximum.

Kβ spectra for resonant excitation. The Kβ spectra of HydA1(rai) for resonant excitation depended strongly on the excitation energy (Fig. 3B), indicating high selectivity for $[2Fe]_H$ and $[4Fe4S]_H$ in the pre-edge absorption. The HydA1(rai) spectrum for excitation at 7111.5 eV closely resembled that of HydA1(apo) and the spectrum for excitation at 7114.5 eV was similar to that of PDT(2Fe). Weighted ratio calculation of the PDT(2Fe) and HydA1(apo) spectra revealed maximal relative contributions of $[2Fe]_H$ in the Kβ′ region up to ~90% (enrichment ~2.7) and of $[4Fe4S]_H$ in the $K\beta^{1,3}$ region up to ~70%. Accordingly, only small contributions from the respective second species spectra needed to be subtracted to yield the pure resonant Kβ spectra of the $[2Fe]_H$ and $[4Fe4S]_H$ units (Fig. 3B).

Site-selective XANES spectra. The K-edge absorption (XANES) reflects the metal oxidation state and the chemical nature and geometry of the ligands (Fig. 4A). The Kα-detected XANES of HydA1(apo) showed a typical shape for FeS clusters and the XANES of PDT(2Fe) differed by shape variations and a higher edge energy. The HydA1(rai) Kα-XANES reflected the dominance of $[4Fe4S]_H$. XANES spectra of HydA1(apo), FDX(4Fe), and PDT(2Fe) for detection energies at the Kβ′ and $K\beta^{1,3}$ maxima revealed a similar main edge shape and energy, which was also similar to the Kα-detected spectrum (Fig. S3†). However, in the spectra of HydA1(apo) and FDX(4Fe), pronounced pre-edge features were observed for $K\beta^{1,3}$ detection, which vanished for Kβ′ detection, whereas the pre-edge of PDT(2Fe) was similar at both detection energies (Fig. S3†). This showed that for homogeneous samples, the mode of emission detection was irrelevant for the XANES spectrum and was in agreement with the hs Fe(II/III) ions in HydA1(apo) and FDX(4Fe) and the ls Fe(I) ions in PDT(2Fe), emphasizing the high spin-selectivity of the Kβ′ and $K\beta^{1,3}$ emission regions for resonant excitation. For HydA1(rai), Kβ-detection at energies, for which dominance of $[4Fe4S]_H$ or $[2Fe]_H$ was expected, yielded XANES spectra showing considerable shape differences (Fig. 4A).

Calculation of weighted Kβ-XANES difference spectra was carried out, using the energy-dependent relative species contributions from the non-resonant Kβ emission analysis (Fig. 3A). The two spectra derived each for $[4Fe4S]_H$ and $[2Fe]_H$ differed only slightly (Fig. S3-A†) and thus were averaged. We consider the resulting spectra as being close to the pure XANES of $[2Fe]_H$ and $[4Fe4S]_H$ (Fig. 4A). Notably, the spectra for narrow-band Kβ-detection showed better resolved edge features than the broad-band Kα-detected spectra. The edge energy for $[4Fe4S]_H$ of 7119.1 ± 0.1 eV was centered between those for S-coordinated Fe(II) and Fe(III) compounds (7117.5 eV and 7120.9 eV, Fig. S3-A†), suggesting an $Fe(II)_2Fe(III)_2$ oxidation state of the cubane cluster in HydA1(rai). A more pronounced shoulder compared to PDT(2Fe) was observed in the main edge rise of $Fe_2S_2(CO)_6$ and $[2Fe]_H$ (Fig. S3-A†), which suggested that this feature was proportional to the number of (CO) ligands, due to electronic transitions into MOs with (CO) character. A higher number of (CO) ligands per iron atom presumably resulted from the presence of an Fe–Fe bridging (CO) in $[2Fe]_H$.

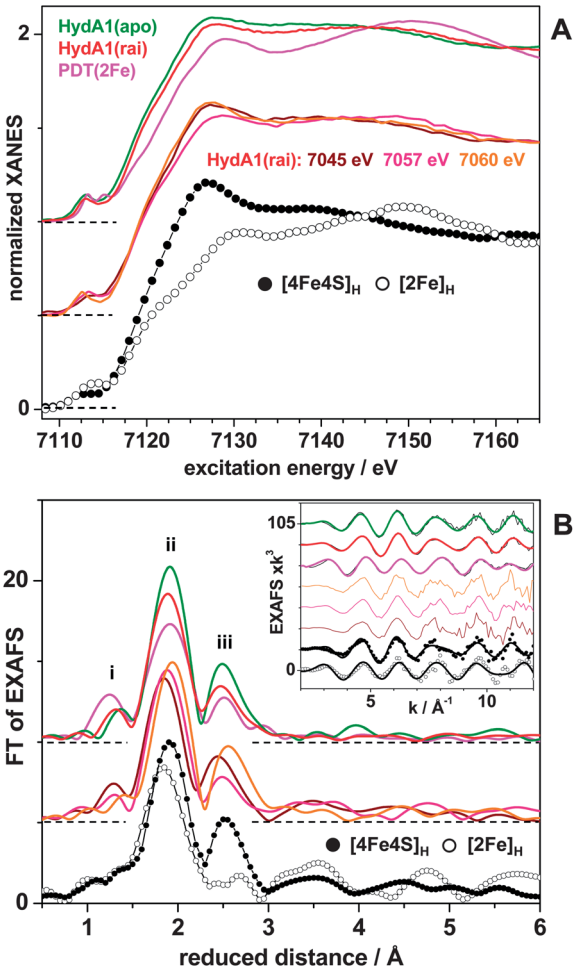

Fig. 4 Site-selective XANES and EXAFS spectra. (A) XANES spectra. Top: conventional Kα-emission detected spectra. Middle: spectra of HydA1 detected at the indicated Kβ-emission energies. Bottom: spectra representing the mean of each two difference spectra (Fig. S3-B†), which were obtained by subtraction of spectra weighted according to the relative sub-cluster contributions (Fig. 3A) and rescaling ($[4Fe4S]_H$ = {(HydA1(rai)$_{7045}$ − HydA1(rai)$_{7057}$ × 0.48) × 1.92 + (HydA1(rai)$_{7060}$ − HydA1(rai)$_{7057}$ × 0.53) × 2.13}/2; $[2Fe]_H$ = {(HydA1(rai)$_{7057}$ − HydA1(rai)$_{7045}$ × 0.68) × 3.12) + (HydA1(rai)$_{7057}$ − HydA1(rai)$_{7060}$ × 0.70) × 3.33}/2). Spectra were vertically shifted for comparison. (B) EXAFS spectra (Fourier-transforms of EXAFS data in the inset). The shown Kα- (top) and Kβ-detected (middle) spectra correspond to the XANES data in (A). The bottom spectra represent the mean of difference spectra (Fig. S4†) derived for the differences of Kβ-detected spectra by the same procedure as explained under (A) and using differences of Kβ- and Kα-detected spectra in addition (allowing for a ±5% variation in the relative sub-cluster contributions for fine adjustment, see the legend of Fig. S4†). Inset: thin lines, experimental data; thick lines, simulations with parameters in Table 1.

Site-selective EXAFS spectra. EXAFS spectra of the $[4Fe4S]_H$ and $[2Fe]_H$ units of the H-cluster were obtained in a similar way as described above for the HydA1(rai) XANES and the $Fe_2(CO)_9/Fe_2O_3$ mixture. The Kα-detected EXAFS of HyA1(rai) revealed features similar to those of both PDT(2Fe) and HyA1(apo) (Fig. 4B), due to the similar ligation of iron by, *e.g.*,

(CO)- and S-ligands. EXAFS simulations for PDT(2Fe) well reproduced the interatomic distances in the crystal structure and for HydA1(apo) revealed coordination numbers and Fe–Fe distances typical for a [4Fe4S] cluster, *i.e.* in comparison to FDX(4Fe) (Table S1†). For samples containing only similar, either hs or ls iron sites (in PDT(2Fe), FDX(4Fe) and $Fe^{III}(dedtc)_3$; Fig. S2-B†), respective EXAFS spectra were practically identical for Kα-, Kβ′- or $K\beta^{1,3}$-detection, as were the respective simulation results, and significant site-selectivity hence was not observed for these rather homogeneous samples (Fig. S4-A, Table S1†).

The Kβ′- and $K\beta^{1,3}$-detected EXAFS spectra of HydA1(rai) showed differences, for example with respect to the energies of the Fourier-transform (FT) peaks (i) and (ii), attributable to Fe–C(=O/N) and Fe–S interactions and peak (iii), due to Fe–Fe and multiple-scattering Fe(–C)=O/N contributions[22,99] (Fig. 4B). This suggested that the two units contributed differently to the spectra. Linear combination either of the Kβ-detected spectra at different energies or of the Kα- and Kβ-detected spectra, after weighting according to the energy-dependent contributions of the two sub-units (Fig. 3B), yielded three spectra for $[2Fe]_H$ and four spectra for $[4Fe4S]_H$ (Fig. S4-B†). Signal averaging yielded the mean spectra for iron atoms in the $[2Fe]_H$ and $[4Fe4S]_H$ units (Fig. 4B). The FT-spectrum of the $[4Fe4S]_H$ EXAFS showed a pronounced third peak, due to three ~2.7 Å Fe–Fe distances per iron atom only in this unit. This peak was almost absent in the FT of the $[2Fe]_H$ EXAFS, which revealed a shift of the first peak to shorter distances in addition, due to the shorter Fe–(CO/N) bonds.

Simulations of the HydA1(rai) EXAFS spectra revealed the iron–ligand bond lengths and the Fe–Fe distance in $[2Fe]_H$ (Table 1). Within error limits, the interatomic distances (R) for the Kβ- and Kα-detected spectra were similar. However, the coordination numbers (N) and Debye–Waller parameters ($2\sigma^2$) for the deconvoluted Kβ-detected spectrum showed that it represented the almost pure $[2Fe]_H$ unit. Notably, the FT peak features due to Fe–(CO/N) interactions were less pronounced compared to PDT(2Fe), due to a broader bond lengths distribution in $[2Fe]_H$. For $[4Fe4S]_H$, EXAFS simulations yielded by ~0.08 Å shorter Fe–S and by ~0.1 Å shorter Fe–Fe distances for the Kβ′-spectrum at 7045 eV, compared to the $K\beta^{1,3}$-spectrum at 7060 eV (Table 1). This suggested that iron atoms existed in $[4Fe4S]_H$, which were discriminated by shorter Fe–S bonds and shorter distances to the neighbouring irons and contributed preferentially to the Kβ′-detected EXAFS. $[4Fe4S]_H$ in crystal structures revealed typically 2 (out of a total of 6) Fe–Fe distances, which are longer by ~0.08 Å (Fig. 1), and a similar distance distribution was obtained in the DFT calculations described further below (Table 1). Shorter Fe–S bonds were expected for the Fe(III) ions in $[4Fe4S]_H$.

Valence-to-core transitions. Electronic decay processes from occupied valence levels after non-resonant excitation were monitored in the $K\beta^{2,5}$ emission region (Fig. 5A). The $K\beta^{2,5}$ spectra of HydA1(apo) and FDX(4Fe) were rather similar and the slightly higher line energy suggested a more oxidized [4Fe4S] cluster in HydA1(apo) (Fig. S5†). The PDT(2Fe) spectrum differed from the former two spectra in particular by showing higher emission intensities at lower energies, attributable to decay from MOs with mainly (CO) character.[74] The $K\beta^{2,5}$ emission of HydA1(rai) revealed low-energy features similar to PDT(2Fe) and high-energy features comparable to HydA1(apo). We consider the HydA1(apo) spectrum and the difference HydA1(rai) minus HydA1(apo) as closely resembling the $K\beta^{2,5}$ spectra of $[4Fe4S]_H$ and $[2Fe]_H$ (Fig. 5A). The $K\beta^{2,5}$ emission of $[2Fe]_H$ showed a resolved peak at highest energies, at which preferentially 3d → 1s transitions, *e.g.* from the HOMO, contribute.[72–74]

DFT using the BP86/TZVPP functional/basis-set combination was carried out for geometry-optimization and energy-minimization of model structures for the H-cluster, which were derived on the basis of available crystallographic data and truncating the cysteine side chains (Fig. 1, see Materials and methods for constraints used in the DFT calculations). We considered models with three possible alternative spin orientations on the iron atoms of the cubane cluster (Fig. S7†) and assumed that HydA1(rai) contained a formal $Fe^{II}{}_2Fe^{III}{}_2$–$Fe^{I}{}_2$ state of the H-cluster, in agreement with previous[24] and the present results. On the basis of the structure in Fig. 6, a $K\beta^{2,5}$ sum spectrum was calculated, which reproduced the features of the $K\beta^{2,5}$ emission of HydA1(rai) well (Fig. 5A). Dissection of the sum spectrum into the contributions from the two sub-clusters yielded spectra, which were in good agreement with the site-selective spectra of $[4Fe4S]_H$ and $[2Fe]_H$, allowing assignment of the main $K\beta^{2,5}$ peaks to the dominant MO contributions (Fig. 5A). Structures including the two alternative spin orientations on $[4Fe4S]_H$ (Fig. 6 and S7†) yielded $K\beta^{2,5}$ spectra for $[4Fe4S]_H$ and $[2Fe]_H$ (Fig. S7†) practically identical to the spectra in Fig. 5A. Accordingly, the experimental $K\beta^{2,5}$ spectra were insensitive to the spin orientations in the cubane cluster.

In general, electronic decay occurred from MOs, which were largely localized either on $[4Fe4S]_H$ or $[2Fe]_H$ (Fig. 5A). For $[4Fe4S]_H$, the peak at lowest energies (~7098 eV) was dominated by MOs with mainly S s character whereas the high-energy peak (~7108 eV) comprised contributions mainly from MOs with S p (at lower energies) or Fe d (at higher energies) character. For $[2Fe]_H$, the two peaks at lowest energies (~7100 eV, ~7103 eV) were dominated by MOs with (CO)s,p character, a peak at ~7107 eV showed mainly S s,p contributions from the bridging adt ligand and minor (CN) contributions, and the highest energy peak was due mainly to decay from Fe d levels (see below). The calculated $K\beta^{2,5}$ spectra for the proximal (Fe_p) and distal (Fe_d) iron atoms of $[2Fe]_H$ were quite similar and the slightly higher emission intensity at low energies for Fe_d reflected the shorter bond of the bridging (CO) at this iron. The good agreement between the experimental and calculated $K\beta^{2,5}$ spectra revealed that the H-cluster in HydA1(rai) was well described by a structure (Table S2†) with a formal $Fe(II)_2$-$Fe(III)_2Fe(I)_2$ oxidation state that exhibits an adt bridging ligand, an asymmetrically Fe–Fe bridging (CO) ligand, and an apical vacant site at Fe_d (Fig. 6).

Core-to-valence transitions. The whole resonant inelastic X-ray scattering (RIXS) plane made up by the Kβ-emission and pre-edge absorption spectral regions was collected (Fig. S6†). This facilitated selection of Kβ′ and $K\beta^{1,3}$ emission energies,

Table 1 EXAFS simulation parameters. Simulation results correspond to spectra in Fig. 4B and S4† and are compared to values from our DFT calculations and H-cluster crystal structures indicated by their PDB entry codes. *N*, coordination number; *R*, interatomic distance, $2\sigma^2$, Debye–Waller parameter; R_F, weighted fit error sum.[64] Values in parentheses show the range of Fe–S and Fe–Fe distances in the DFT and crystal structures. (*) *N* was fixed in the fit procedures. EXAFS spectra were measured either using Kα detection or correspond to weighted difference spectra for Kα and/or Kβ detection at the indicated energies (see Fig. 4 and S4†). Values in italics correspond to two parameter sets for $[4Fe4S]_H$ ($4Fe_a$ and $4Fe_b$) obtained for Kβ′ or $K\beta^{1,3}$ detection; values in bold represent parameters derived for averaged spectra of $[2Fe]_H$ and $[4Fe4S]_H$. EXAFS fits for $[2Fe]_H$ spectra of HydA1(rai) included a further Fe(–C)═O/N multiple scattering shell ($N/R/2\sigma^2$) for Kα- (1/3.01/5) and Kβ-detection (3/2.85 ± 0.4/5); parameters were (3/2.98/—) for the 3C8V and DFT structures

		N [per Fe]/R [Å]/$2\sigma^2 \times 10^3$ [Å^2]			
Sample	Method	Fe–C(═O/N)	Fe–S	Fe–Fe	R_F [%]
HydA1(apo)	EXAFS Kα $[4Fe4S]_H$	—	4*/2.28/7	3*/2.71/20	13.5
	Crystal (3LX4) $[4Fe4S]_H$	—	4/2.29/—	3/2.74/—	—
	$4Fe_a$			(1.5/2.71/—	
	$4Fe_b$			1.5/2.76/—)	
HydA1(rai)	EXAFS Kα $[4Fe4S]_H[2Fe]_H$	1*/1.86/3	3.5*/2.25/11	0.5*/2.56/2	6.3
				2*/2.72/5	
	EXAFS $K\beta_{7057}$-Kα	3*/1.84/2	2.5*/2.23/6	1*/2.55/2	23.4
	EXAFS $K\beta_{7057-(7045+7060)}$	3*/1.83/9	2.5*/2.22/3	1*/2.57/2	21.7
	EXAFS $[2Fe]_H$	**3*/1.84/7**	**2.5*/2.22/5**	**1*/2.56/2**	**18.2**
	DFT $[2Fe]_H$	3/1.86/—	2.5/2.35/—	1/2.59/—	—
	EXAFS $K\beta_{7045}$-Kα	—	4*/2.26/8	3*/2.66/15	22.8
	EXAFS $K\beta_{7045-7057}$	—	4*/2.27/7	3*/2.66/10	21.4
	EXAFS $K\beta'_{mean}$ ($4Fe_a$)	—	*4*/2.26/8*	*3*/2.66/12*	*19.5*
	EXAFS $K\beta_{7060}$-Kα	—	4*/2.33/6	3*/2.78/11	18.8
	EXAFS $K\beta_{7060-7057}$	—	4*/2.34/6	3*/2.77/9	19.5
	EXAFS $K\beta^{1,3}{}_{mean}$ ($4Fe_b$)	—	*4*/2.33/6*	*3*/2.77/8*	*17.4*
	EXAFS $[4Fe4S]_H$	**—**	**4*/2.29/6**	**3*/2.72/12**	**14.5**
	DFT $[4Fe4S]_H$	—	4/2.28/—	3/2.70/—	—
	$4Fe_a$		(2/2.26/—	(2/2.67/—	
	$4Fe_b$		2/2.30/—)	1/2.77/—)	
Bacterial [FeFe]-hydrogenases	Crystal (3C8V) $[2Fe]_H$	3/1.86/—	2.5/2.32/—	1/2.55/—	—
	Crystal (1HFE) $[4Fe4S]_H$	—	4/2.31/—	3/2.70/—	—
	$4Fe_a$			(2/2.69/—	
	$4Fe_b$			1/2.75/—)	

which showed the highest relative contributions of $[2Fe]_H$ and $[4Fe4S]_H$ to the pre-edge absorption spectra (Fig. 5B). Thereby, pre-edge spectra of HydA1(rai) were obtained, which for Kβ′-detection to some extent resembled the PDT(2Fe) spectrum and for $K\beta^{1,3}$-detection were similar to the HydA1(apo) spectrum (compare Fig. 5B and S3-A†), emphasizing the high selectivity of the Kβ′ emission for the low-spin iron. Subtraction of only small amounts of the respective other spectrum, using the relative contributions determined from the resonant Kβ spectra, thus yielded the pure core-to-valence excitation spectra for $[4Fe4S]_H$ and $[2Fe]_H$ (Fig. 5B).

Calculation by time-dependent DFT of the electronic transitions accounting for the pre-edge absorption of the structure in Fig. 6 yielded a sum spectrum, which well reproduced the three main peak features in the non-selective Kα-detected pre-edge spectrum of HydA1(rai) (Fig. 5B). Dissection of the sum spectrum into the contributions from the two sub-clusters yielded spectra in very good agreement with the experimental $[4Fe4S]_H$ and $[2Fe]_H$ spectra (Fig. 5B). The spectra of $[4Fe4S]_H$ calculated for structures including the three alternative spin states of the cubane showed relatively small differences (Fig. S7†). The absorption peak at ~7112.5 eV was due to MOs with Fe d character mainly of the iron (Fe1), to which the cysteine bridging to $[2Fe]_H$ was coordinated, and to the iron (Fe2) opposed to Fe_1 whereas the shoulder feature at ~7113.5 eV was dominated by Fe d MOs mainly on the other two irons (Fe3, Fe4) (Fig. 5B). The shoulder feature seemingly was best reproduced in the calculated spectrum for the structure in Fig. 6 whereas the models with the two alternative spin states yielded less structured $[4Fe4S]_H$ pre-edge spectra (Fig. S7†). The $[2Fe]_H$ pre-edge spectra for the three structures with alternative spin states were practically identical (Fig. S7†). Remarkably, the spectra for Fe_p and Fe_d in $[2Fe]_H$ were very different, reflecting the asymmetric ligation of the two iron species. For $[2Fe]_H$, the lowest-energy peak (~7112.5 eV) revealed contributions almost exclusively from MOs with d-character of Fe_d, the peak at ~7113.5 eV was due to about equal contributions from Fe d-dominated MOs of both iron atoms, and the highest energy feature (~7114.5 eV) was attributable to transitions into MOs with mainly (CO)s,p character and dominated by Fe_p.

Sorting of calculated excitation transitions either according to the core level (1s) contributions (Fig. 5) or to the virtual level (target MOs) contributions revealed that excitation of a 1s electron of either Fe_p or Fe_d resulted in transitions to MOs with

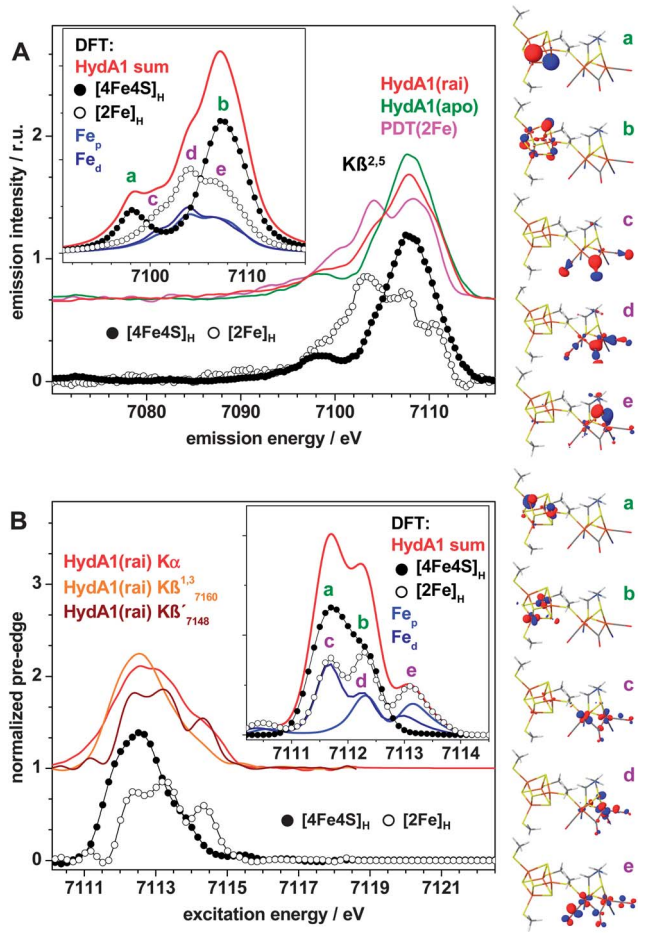

Fig. 5 Valence-to-core and core-to-valence electronic transitions for the H-cluster. (A) $K\beta^{2,5}$ emission spectra for non-resonant excitation (7600 eV) normalized to unity area. Spectra of the indicated samples (top) are compared to spectra (bottom) for the sub-complexes ($[4Fe4S]_H$ = HydA1(apo), $[2Fe]_H$ = (HydA1(rai) × 6 − HydA1(apo) × 4) × 0.5). Inset: DFT-calculated $K\beta^{2,5}$ spectra from Gaussian broadening (FWHM 3 eV) of stick spectra (Fig. 7A) for the whole H-cluster (sum), for $[4Fe4S]_H$ and $[2Fe]_H$, and for the proximal (Fe_p) and distal (Fe_d) irons in $[2Fe]_H$. (B) Isolated pre-edge absorption spectra for the indicated detection modes and energies (top, see Fig. S6† for RIXS plane data) and spectra (bottom) for the sub-complexes ($[4Fe4S]_H$ = $(HydA1(rai)_{7060} - HydA1(rai)_{7045} \times 0.1) \times 1.11$, $[2Fe]_H$ = $(HydA1(rai)_{7045} - HydA1(rai)_{7060} \times 0.25) \times 1.33$). Inset: pre-edge spectra from Gaussian broadening (FWHM 0.5 eV) of stick spectra from DFT (Fig. 7B) for the sub-complexes. Calculated spectra in (A) and (B) were derived using the model in Fig. 6 and correspond to transitions sorted according to their Fe1s contributions. Overall similar spectra were calculated for models with alternative spin orientations in $[4Fe4S]_H$ (Fig. S7†). Right panel: DFT-optimized model of the H-cluster (Fig. 6) and MOs corresponding to peak features a–e in (A) and (B).

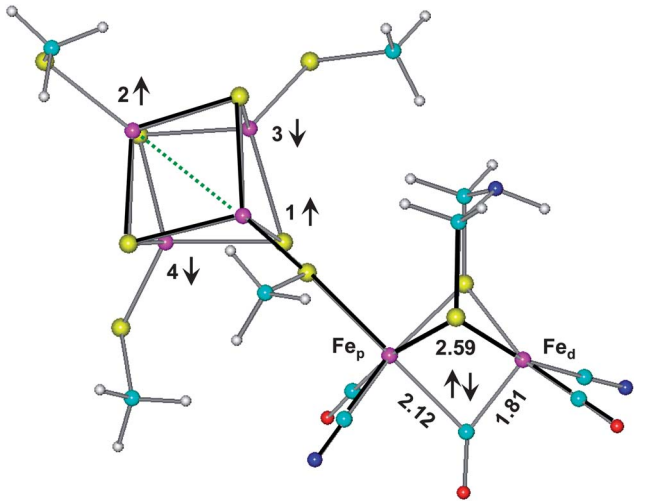

Fig. 6 H-cluster model structure from DFT. The coordinates are listed in Table S2.† Color code: Fe, magenta; S, yellow; O, red; N, blue; C, cyan; H, white. Fe_p–Fe_d and further distances are given in Å. Arrows denote α (up) or β (down) net spins on $[4Fe4S]_H$ and spin pairing on $[2Fe]_H$. Particularly long Fe1–Fe2 (2.80 Å, green dotted line) and Fe3–Fe4 (2.74 Å) distances in $[4Fe4S]_H$ were observed, which were similar to distances determined from the EXAFS analyses (Table 1). A similar model with α-spins on Fe2 and Fe4 and β-spins on Fe1 and Fe3 showed long Fe1–Fe2 (2.88 Å) and Fe1–Fe3 (2.79 Å) distances (Fig. S7†), which exceeded the Fe–Fe distances from EXAFS. Further details are given in the test.

Fe d-character mainly of $[4Fe4S]_H$, *i.e.* to the LUMO (Fig. 7). Furthermore, the latter sorting showed the contributions from the four iron atoms, the μ-S bridges, and the terminal CH_3 groups of $[4Fe4S]_H$ and from the two iron atoms, the adt bridge, and the (CO) and (CN) ligands of $[2Fe]_H$ to the $K\beta^{2,5}$ emission and pre-edge absorption spectra of the H-cluster model structure (Fig. 7). Accordingly, the experimental $K\beta^{2,5}$ spectrum around ~7104 eV and the pre-edge absorption at highest energies is expected to be particularly sensitive to changes of the (CO) ligands at $[2Fe]_H$ and the $K\beta^{2,5}$ spectrum at lowest energies mostly affected by changes at the μ-S bridges in $[4Fe4S]_H$, for example in response to redox changes.

Protonation of $[2Fe]_H$ in the reduced state of the H-cluster has been suggested. We calculated the pre-edge absorption and $K\beta^{2,5}$ emission spectra for a model structure similar to that in Fig. 6, but carrying a proton at the apical position on Fe_d in addition (Fig. S8†). The resulting spectra of the protonated species, in particular for the pre-edge absorption, significantly differed from the spectra of the unprotonated site (Fig. S8†) and were in pronounced disagreement with the experimental spectra of $[2Fe]_H$ (Fig. 5). This supported the notion that the H-cluster in the reduced state does not carry a H-species at Fe_d.

HOMO–LUMO energy gap and Fe d degeneracy. The three H-cluster models from DFT with different spin orientations on $[4Fe4S]_H$ overall showed similar structures and in particular the same Fe–Fe distance (2.59 Å) in $[2Fe]_H$ (Fig. S7†). However, the Fe–Fe distance distribution within $[4Fe4S]_H$ depended on the spin state. A structure with α (up) spins on Fe1 and Fe4 (and β (down) spins on Fe2 and Fe3) showed only relatively short (≤2.71 Å) Fe–Fe distances and lacked significantly longer distances in the cubane (Fig. S7,† structure c). This was not in agreement with the observation of long Fe–Fe distances in the site-selective EXAFS data (Table 1) and therefore this model was not considered further. The other two structures both revealed a long distance (2.80–2.88 Å) between Fe1 and Fe2 and a second long distance either between Fe3 and Fe4 (2.74 Å) for α-spins on Fe1 and Fe2 (Fig. 6; Fig. S7,† structure a) or between Fe1 and Fe3

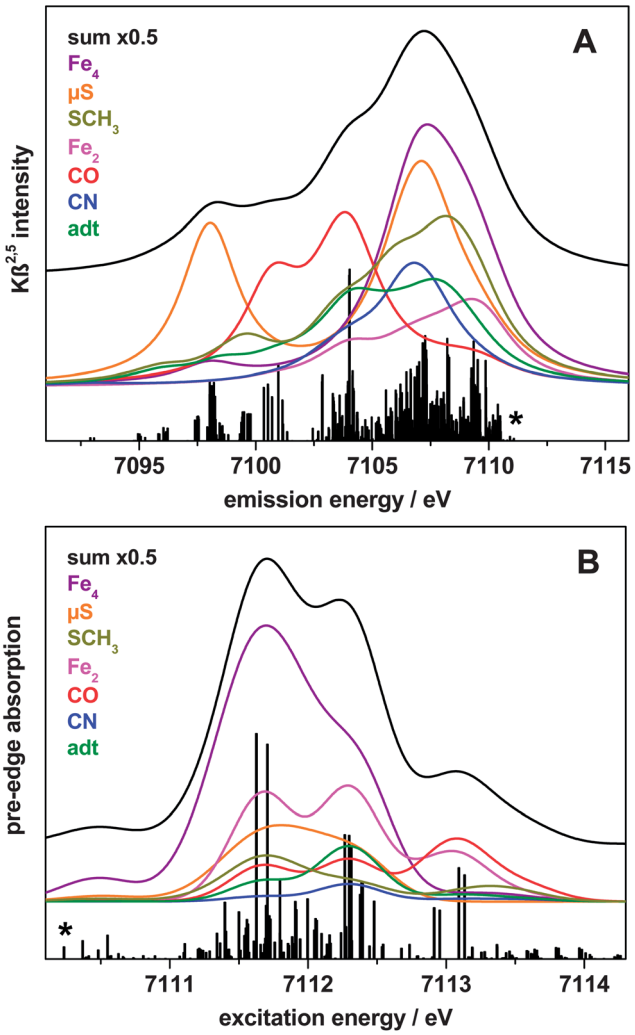

Fig. 7 Metal and ligand contributions to Kβ^{2,5} emission and pre-edge absorption spectra from DFT. Data are for the model in Fig. 6 and similar spectral contributions were observed irrespective of the spin orientations in $[4Fe4S]_H$ (Fig. S7†). (A) Kβ^{2,5} spectra and (B) pre-edge absorption spectra calculated using Gaussian broadening of respective stick spectra (scaled for display) for the indicated components of the H-cluster. Calculated spectra in (A) and (B) were derived by assigning transitions to the species according to their target MO contributions. Asterisks mark sticks corresponding to the HOMO → Fe 1s (A) and Fe 1s → LUMO (B) electronic transitions.

(2.79 Å) for α-spins on Fe2 and Fe4 (Fig. S7,† structure b). However, the long Fe–Fe distances in the latter model were considerably larger than the distances determined from the EXAFS analyses whereas the distances for the structure in Fig. 6 were in better agreement with the experimental data.

Irrespective of the spin orientations on $[4Fe4S]_H$ in the model, the HOMO showed predominant d(z^2) character of the distal iron (~45%) of $[2Fe]_H$ and aligned roughly with the direction of the Fe_d–(CO) bond to the bridging ligand. The LUMO was considerably delocalized over $[4Fe4S]_H$ (Fig. 8). The HOMO–LUMO energy difference was estimated as 0.3 ± 0.2 eV from the low- and high-energy inflection points in the first derivatives (not shown) of the experimental Kα-detected pre-edge absorption (Fig. 5B) and Kβ^{2,5} emission spectra (Fig. 5A).[72,73] The DFT calculations yielded values in the range of 0.17–0.21 eV for the two structures with the more realistic spin orientations in the cubane (Fig. 8; S7a and b†). However, our earlier studies on diiron complexes have shown that the used DFT approach underestimates the energy difference by a factor of ~1.3.[72–74] Application of this factor yielded a gap in the range of 0.22–0.27 eV, in even better agreement with the experiment.

The MOs on $[4Fe4S]_H$ (not shown) showed relatively low Fe d-characters (<30%), accordingly considerable S-character, and were generally rather delocalized over the whole cubane. The sum of the four iron spins in $[4Fe4S]_H$ was close to zero (<0.13) due to the compensation of two α by two β net spins (Fig. 6 and S7†). The two iron atoms of $[2Fe]_H$ carried almost zero net spin (<0.17). The shapes and energies of unoccupied and occupied MOs with predominant Fe d character revealed that the d-level degeneracy for Fe_p to some extent resembled an octahedral ls Fe(II) ion whereas Fe_d in tendency was more close to a square-pyramidal ls Fe(0) ion (Fig. 9). This was particularly apparent from inspection of the MOs with d(z^2) and d($x^2 - y^2$) characters at the highest energies. The MO configuration thus reflected the asymmetric coordination at the two iron atoms and was in agreement with a more reducing character of Fe_d. Two electrons from each Fe_p and Fe_d apparently can be considered as pairing in an MO with Fe–Fe bonding character (Fig. 9). The almost zero

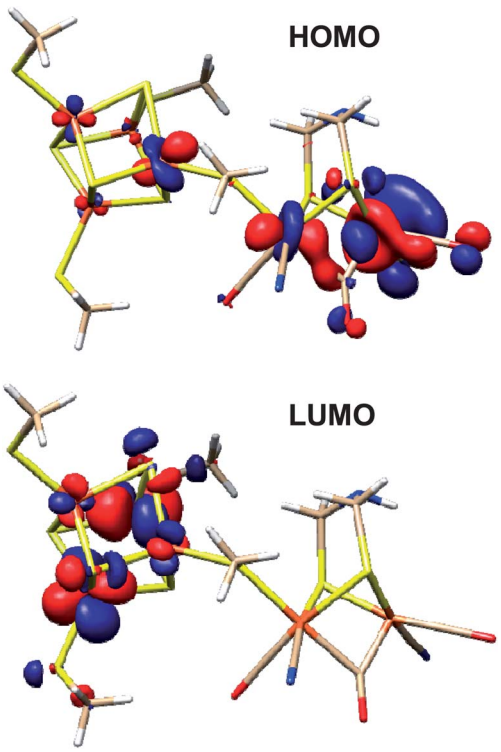

Fig. 8 HOMO and LUMO in the H-cluster model for HydA1(rai). MO energies and metal/ligand characters: HOMO, −0.34 eV, 16% Fe_p, 45% Fe_d, 23% $[2Fe]_H$ ligands, and 16% $[4Fe4S]_H$; LUMO, −0.17 eV, 84% Fe_4, 8% $[4Fe4S]_H$ ligands, and 8% $[2Fe]_H$. Data are for the model in Fig. 6, for HOMO and LUMO configurations in DFT models with alternative spin orientations in $[4Fe4S]_H$ see Fig. S7.†

net spin on $[2Fe]_H$ and the spin compensation in $[4Fe4S]_H$ thus accounted for the observed non-paramagnetic character of the H-cluster in HydA1(rai).

Discussion

We used the spin-polarization of the Kβ′ and Kβ[1,3] X-ray fluorescence emission lines to obtain pre-edge absorption (1s → 3d), XANES and EXAFS spectra, as well as the excitation energy dependent contributions of resonant electronic transitions (1s → 3d) to yield Kβ emission spectra for resonant excitation in a site-selective approach, individually for the $[4Fe4S]_H$ and $[2Fe]_H$ sub-complexes of the H-cluster in HydA1 [FeFe]-hydrogenase protein. In addition, comparison of XES and XAS spectra of HydA1 containing the complete H-cluster and of apo-HydA1 binding only $[4Fe4S]_H$ provided Kβ (3p → 1s) and Kβ[2,5] (3d → 1s) emission spectra for non-resonant excitation for the two sub-complexes. Derivation of site-selective XAS spectra for the H-cluster was complicated by *a priori* unknown energy-dependent spectral contributions of the sub-complexes to the Kβ emission. In a site-selectivity XAE study on Prussian Blue, a numerical method for spectral deconvolution was suggested, however, yielding non-unique solutions.[71] Here, we remedied this problem by selection of suitable iron reference compounds as Kβ emission standards, facilitating determination of the spectral contributions of the sub-complexes with an estimated accuracy of better than ±10%. Discrimination of low- and high-spin iron sites, further distinguished by different coordination environments, thereby was achieved for the protein-bound metal center.

The site-selective XANES clearly revealed the different coordination environments at the iron atoms in $[4Fe4S]_H$, featuring Fe–S bonds only, and in $[2Fe]_H$, dominated by the (CO/N) ligands. Redox state changes at either sub-complex thus may be monitored by utilizing the oxidation state dependence of the Fe K-edge energy.[32,100] EXAFS analysis yielded an Fe–Fe distance of ~2.56 Å in $[2Fe]_H$, which is similar to the distances observed in crystal structures of bacterial [FeFe]-hydrogenases[25,27] and in non-site-selective EXAFS data.[17,22,29] A similar distance was observed in the DFT model structures. Fe–S and Fe–C(O/N) bond lengths were determined in addition. The pronouncedly structured core-to-valence spectrum was well reproduced by the DFT calculations, thus revealing the Fe_p and Fe_d contributions to the electronic transitions to unoccupied MOs (1s → 3d) and facilitating discrimination between the two iron atoms in $[2Fe]_H$. Fe_d contributed mostly at lowest excitation energies, which suggests that for example hydride or ROS binding at open coordination sites or (CO) geometry changes[24,31] would be specifically detectable.

Our DFT approach yielded model structures of the reduced H-cluster, showing a bridging (CO) ligand in $[2Fe]_H$, in agreement with recent infrared data,[24,47] and an open coordination site at Fe_d. These features, which were independent of the spin

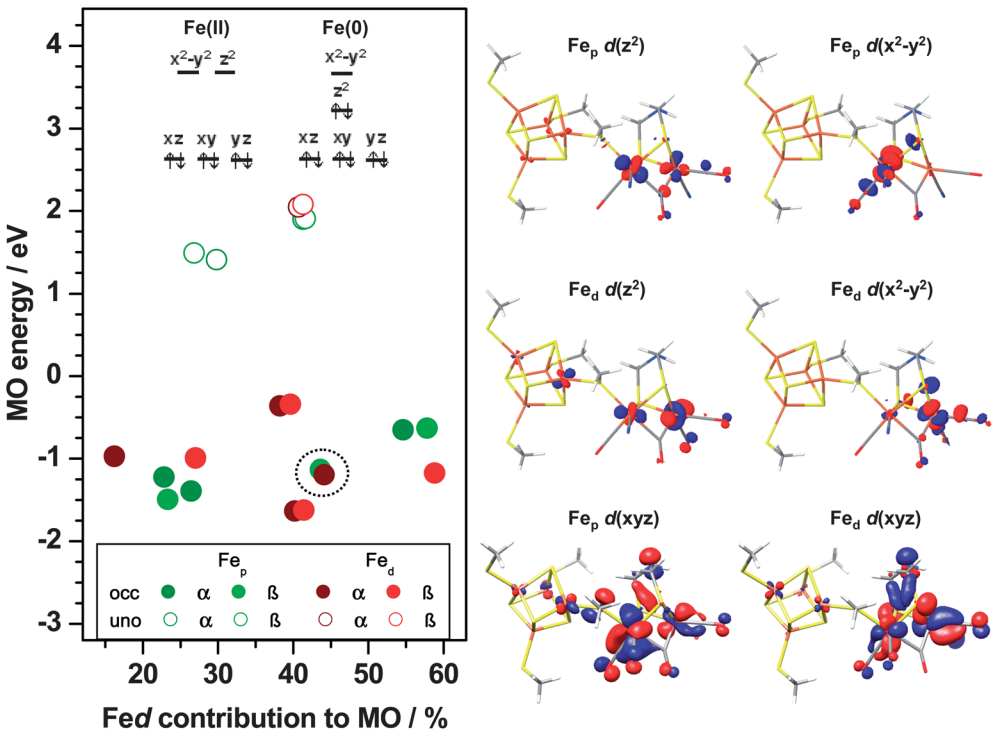

Fig. 9 Configurations of MOs with Fe d character from DFT. Data are for the model in Fig. 6 and similar MO properties (not shown) were observed for a model with alternative spin orientations on $[4Fe4S]_H$ (Fig. S7,† model b). MOs in the left panel correspond to the seven singly occupied (occ, solid circles) and four unoccupied (uno, open circles) MOs with highest α- or β-spin Fe_p or Fe_d character around the zero energy level. Inset: ideal ls O_h Fe(II) and C_{4v} Fe(0) d-level degeneracies in an atomic picture. The dashed circle marks the two MOs shown at the bottom of the right panel. The right panel shows MOs with the highest respective Fe d characters in the model structure. The MOs in the bottom part were calculated using a lower cut-off value to emphasize their Fe–Fe bonding character.

configuration in the cubane cluster, were essential for reproduction of the main X-ray spectral properties. A model structure containing a proton bound to Fe_d yielded spectra, which were not in agreement with the experimental data. Accordingly, we propose that Fe_d in the reduced state is unprotonated. The possibility remains that the protonation state depends on sample conditions, for example on the pH. HydA1 is actively producing H_2 at the pH of 8 in our samples,[101,102] but pH variation could affect the relative proportions of states accumulating under steady state conditions.[24,47,48] Further investigations of pH effects on the H-cluster structure are required to clarify this issue.

Earlier DFT studies on H-cluster models have shown that for example variations of the functional/basis-set combination in the DFT approach yielded globally similar structures[42,44,48,103–105] and mostly caused a systematic bias in the absolute energies of the structures and the energy differences between MOs.[19,45] Notably, in some of the earlier DFT studies truncated H-cluster models including only the $[2Fe]_H$ unit have been used, the bridging ligand in $[2Fe]_H$ was modeled as pdt ($(SCH_2)_2O$) or odt ($(SCH_2)_2CH_2$) instead of adt ($(SCH_2)_2NH$),[38,106] an apical oxygen species was bound to Fe_d, or the assumed oxidation state was not in agreement *i.e.* with magnetic resonance data. In the light of the considerable delocalization of MOs over the whole H-cluster, including the adt ligand, and the likely absence of an apical ligand at Fe_d in the anaerobically reduced site in the present study, we consider the choice of appropriate H-cluster models as critical for comparison between spectroscopic and calculated data. This is highlighted by the results of previous DFT calculations of infrared vibrational frequencies of the (CO) and $(CN)^-$ ligands at $[2Fe]_H$ and comparison to experimental data that, for the reduced H-cluster, have favoured a terminal (CO) at Fe_d and a bridging proton for a truncated model[42] or structures with a bridging (CO) with or without a terminal proton at Fe_d for complete models.[41]

A recent DFT study on the reaction cycle of H_2 formation suggested a structure with a bridging (CO) and a terminal proton at Fe_d for the reduced H-cluster.[48] Our comparison of calculated and experimental XAE spectra favours a structure with a bridging (CO), in agreement with recent infrared data,[24,47] and an open site at Fe_d as the main species in our reduced HydA1 samples. Notably, consideration of XAE spectra of sulfur ligands to iron could potentially contribute to further refinement of the electronic structure and possible sulfur ligand protonation,[105] but will be difficult due to overlapping signals from S-containing amino acids not bound to the H-cluster. In conclusion, we consider the good agreement between the experimental XAE data and the DFT-calculated spectra as compelling evidence, that our model provides a suitable representation of both the molecular and electronic configurations of the reduced H-cluster.

The valence-to-core ($K\beta^{2,5}$) emission for non-resonant excitation, in conjunction with the DFT calculations, revealed the specific energy-dependent contributions of electronic decay from MOs with either predominant metal (d) or ligand (*e.g.* (CO)) character, selectively for $[4Fe4S]_H$ and $[2Fe]_H$. In previous studies we have demonstrated the sensitivity of the $K\beta^{2,5}$ emission for detection of iron-bound hydride, which was further enhanced for resonant excitation.[73,74] Collection of resonant-excitation $K\beta^{2,5}$ spectra for dilute HydA1 protein samples here was not attempted due to the extremely low intensity of the $K\beta^{2,5}$ emission and to the small HOMO–LUMO energy gap, which causes overlap of the elastically scattered incident X-rays with the high-energy $K\beta^{2,5}$ emission. However, even in non-resonant $K\beta^{2,5}$ spectra, the effects for example of (CO) ligation changes at $[2Fe]_H$ should be resolvable.

Remarkably, even fine structural details in the $[4Fe4S]_H$ unit seemingly were resolved by site-selective EXAFS. The underlying multiplet structure in the Kβ emission,[107,108] which apparently causes different spectral contributions of the formal Fe(II) and Fe(III) species of the cubane in the $K\beta'$ and $K\beta^{1,3}$ regions, however, needs to be elucidated. Two main Fe–Fe distances of ~2.67 Å and ~2.77 Å were determined and smaller Fe–S bond lengths differences were detected. In the H-cluster crystal structures, longer and shorter Fe–Fe distances in the cubane also were observed, but their location was variable (Fig. 1). Our calculations revealed that the distribution of longer and shorter Fe–Fe distances in $[4Fe4S]_H$ depends on the spin orientations. A model including α-spins on Fe1 and Fe4 showing only short Fe–Fe distances in the cubane thus was unlikely. Models with α-spins on (a) Fe1 and Fe2 or (b) Fe2 and Fe4 both showed a long Fe1–Fe2 distance, as observed in crystal structures (Fig. 1), but a second long distance was observed between either (a) Fe3 and Fe4 or (b) Fe1 and Fe3. At present, we favour model (a) because the spectral features of the calculated pre-edge absorption of $[4Fe4S]_H$ were better in agreement with the experimental data, as were the distance values for the long Fe–Fe vectors. For this model (Fig. 6), the higher occupancy of Fe d–dominated MOs tentatively places an Fe(II) ion at the Fe2 position in $[4Fe4S]_H$.

The structural features, such as a bulk-accessible open coordination site at Fe_d, a (CO) ligand blocking the Fe–Fe bridging position, and a pendant nitrogen base of the adt in $[2Fe]_H$, seemingly prepare the H-cluster for hydride binding in response to electron uptake. The HOMO and LUMO energies have been shown to be related to the first oxidation and reduction potentials in diiron complexes.[73] The LUMO location on $[4Fe4S]_H$ suggests that this site is the entrance for electron donation. The more oxidizing character of Fe_p prepares this iron for accepting the electron from $[4Fe4S]_H$. Fe_d with an occupied $d(z^2)$ level oriented along the axis connecting the bridging (CO) with the apical open coordination site is pre-set for electron donation to protons delivered from the bulk. This could favour formation of a (transient) terminal hydride at Fe_d, possibly stabilized by hydrogen bonding to the adt nitrogen.[13–15,48] Site-directed mutagenesis on HydA1 has further supported a role of the amine base in proton management.[109–112]

We found an experimental value for the HOMO–LUMO energy difference of only ~0.3 eV for the H-cluster, which was supported by DFT. This gap is about 10-times smaller than values observed for diiron model complexes, in which both the HOMO and the LUMO show predominantly Fe d character and thus are localized mostly at the two iron atoms.[72–74] The addition of the cubane cluster to the diiron active site in the H-cluster leads to a small energy gap and localization of the LUMO on

$[4Fe4S]_H$ and of the HOMO on $[2Fe]_H$ in the reduced state. The close connection between the two sub-complexes thus may be regarded as nature's solution to the problem how oxidation and reduction of the catalyst at similar redox potentials matching those of the natural redox partner, the ferredoxin PetF,[110] can be achieved. Apparently, this facilitates thermodynamically reversible H_2 turnover at negligible electrochemical overpotentials as observed in the [FeFe]-hydrogenases.[102,113,114]

We tentatively incorporated our H-cluster structure into the crystal structure of apo-HydA1 protein[30] (Fig. S9†). This showed that both $[2Fe]_H$ and $[4Fe4S]_H$ are close to the protein surface and Fe_d is accessible from the bulk phase. Such a configuration is in agreement with the role of PetF as the native electron donor to the H-cluster[101,115] and with the high efficiency of electron donation to HydA1 immobilized on conductive materials.[116–118] It also accounts for rapid access of inhibitors such as exogenously added O_2,[17,18] (CO),[102,119] or formaldehyde[120,121] to $[2Fe]_H$. New prospects to study activity inhibition and H_2 formation at the molecular level now are offered by the ability to reconstitute the HydA1 apo-enzyme with synthetic diiron complexes, providing full activity in some cases.[38,39,106] Spin- and site-selective XAE-DFT methods can provide specific insights into changes at diiron catalysts upon their binding to the enzyme and into the reactions of inhibitor and hydride binding at the H-cluster.

Conclusions

A spin- and site-selective XAE-DFT approach was utilized to obtain XAS and XES spectra of the $[4Fe4S]_H$ and $[2Fe]_H$ subcomplexes of the active site in HydA1 [FeFe]-hydrogenase protein for the first time. This provided structural parameters (metal–ligand bond lengths, inter-metal distances) as well as electronic properties (HOMO–LUMO gap, MO configurations) for the individual metal sites and a specific model structure for the H-cluster. We show that fine-structure resolution in the cubane and discrimination of the two iron atoms in the diiron unit is feasible. Our results set the stage for experimental investigations on regio-specific redox chemistry, inhibitor binding, and hydride formation in [FeFe]-hydrogenases.

Abbreviations

adt	Azadithiolate
DFT	Density functional theory
EXAFS	Extended X-ray absorption fine structure
HydA1	[FeFe]-Hydrogenase from *C. reinhardtii*
XAE	Combined XAS and XES spectroscopy
XANES	X-ray absorption near edge structure
XAS	X-ray absorption spectroscopy
XES	X-ray emission spectroscopy

Acknowledgements

M. H. is grateful to the Deutsche Forschungsgemeinschaft (DFG) for a Heisenberg Fellowship and financial support (grants Ha3265/3-1 and Ha3265/6-1). T. H. thanks the Bundesministerium für Bildung und Forschung (BMBF, Design Cells Consortium) and the Volkswagen Foundation (grant LigH2t) for funding. We thank Drs P. Glatzel and J.-D. Cafun at ID26 of ESRF for excellent technical support. M. H. thanks Prof. M. Y. Darensbourg (Texas A & M University) for the generous donation of the PDT(2Fe) complex and the ESRF for granting of a Long Term Project.

References

1 T. Abbasi and S. A. Abbasi, *Renewable Sustainable Energy Rev.*, 2011, **15**, 3034–3040.
2 N. Armaroli and V. Balzani, *ChemSusChem*, 2011, **4**, 21–36.
3 J. D. Holladay, Y. Wang and E. Jones, *Chem. Rev.*, 2004, **104**, 4767–4789.
4 R. Schlögl, *ChemSusChem*, 2010, **3**, 209–222.
5 W. J. Shaw, M. L. Helm and D. L. Dubois, *Biochim. Biophys. Acta*, 2013, **1827**, 1123–1139.
6 A. Le Goff, V. Artero, B. Jousselme, P. D. Tran, N. Guillet, R. Metaye, A. Fihri, S. Palacin and M. Fontecave, *Science*, 2009, **326**, 1384–1387.
7 R. M. Bullock, M. L. Helm, M. P. Stewart, M. R. DuBois and D. L. DuBois, *Science*, 2011, **333**, 863–866.
8 M. Y. Darensbourg, *Nature*, 2005, **433**, 589–591.
9 Y. Lang, R. R. Arnepalli and A. Tiwari, *J. Nanosci. Nanotechnol.*, 2011, **11**, 3719–3739.
10 M. Wang, L. Chen, X. Li and L. Sun, *Dalton Trans.*, 2011, **40**, 12793–12800.
11 L. Xiao, Z. H. Wen, S. Q. Ci, J. H. Chen and Z. He, *Nano Energy*, 2012, **1**, 751–756.
12 C. Tard and C. J. Pickett, *Chem. Rev.*, 2009, **109**, 2245–2274.
13 S. T. Stripp and T. Happe, *Dalton Trans.*, 2009, 9960–9969.
14 D. W. Mulder, E. M. Shepard, J. E. Meuser, N. Joshi, P. W. King, M. C. Posewitz, J. B. Broderick and J. W. Peters, *Structure*, 2011, **19**, 1038–1052.
15 J. C. Fontecilla-Camps, A. Volbeda, C. Cavazza and Y. Nicolet, *Chem. Rev.*, 2007, **107**, 4273–4303.
16 F. A. Armstrong and J. C. Fontecilla-Camps, *Science*, 2008, **321**, 498–499.
17 S. T. Stripp, G. Goldet, C. Brandmayr, O. Sanganas, K. A. Vincent, M. Haumann, F. A. Armstrong and T. Happe, *Proc. Natl. Acad. Sci. U. S. A.*, 2009, **106**, 17331–17336.
18 C. Lambertz, N. Leidel, K. G. Havelius, J. Noth, P. Chernev, M. Winkler, T. Happe and M. Haumann, *J. Biol. Chem.*, 2011, **286**, 40614–40623.
19 M. K. Bruska, M. T. Stiebritz and M. Reiher, *J. Am. Chem. Soc.*, 2011, **133**, 20588–20603.
20 C. Tard, X. Liu, S. K. Ibrahim, M. Bruschi, L. De Gioia, S. C. Davies, X. Yang, L. S. Wang, G. Sawers and C. J. Pickett, *Nature*, 2005, **433**, 610–613.
21 E. M. Shepard, E. S. Boyd, J. B. Broderick and J. W. Peters, *Curr. Opin. Chem. Biol.*, 2011, **15**, 319–327.
22 S. Stripp, O. Sanganas, T. Happe and M. Haumann, *Biochemistry*, 2009, **48**, 5042–5049.

23 W. Lubitz, E. Reijerse and M. van Gastel, *Chem. Rev.*, 2007, **107**, 4331–4365.
24 A. Adamska, A. Silakov, C. Lambertz, O. Rüdiger, T. Happe, E. Reijerse and W. Lubitz, *Angew. Chem., Int. Ed.*, 2012, **51**, 11458–11462; D. W. Mulder, M. W. Ratzloff, E. M. Shepard, A. S. Byer, S. M. Noone, J. W. Peters, J. B. Broderick and P. W. King, *J. Am. Chem. Soc.*, 2013, **135**, 6921–6929.
25 J. W. Peters, W. N. Lanzilotta, B. J. Lemon and L. C. Seefeldt, *Science*, 1998, **282**, 1853–1858.
26 Y. Nicolet, B. J. Lemon, J. C. Fontecilla-Camps and J. W. Peters, *Trends Biochem. Sci.*, 2000, **25**, 138–143.
27 Y. Nicolet, C. Piras, P. Legrand, C. E. Hatchikian and J. C. Fontecilla-Camps, *Structure*, 1999, **7**, 13–23.
28 J. W. Peters and J. B. Broderick, *Annu. Rev. Biochem.*, 2012, **81**, 429–500.
29 I. Czech, S. Stripp, O. Sanganas, N. Leidel, T. Happe and M. Haumann, *FEBS Lett.*, 2011, **585**, 225–230.
30 D. W. Mulder, E. S. Boyd, R. Sarma, R. K. Lange, J. A. Endrizzi, J. B. Broderick and J. W. Peters, *Nature*, 2010, **465**, 248–251.
31 A. Silakov, C. Kamp, E. Reijerse, T. Happe and W. Lubitz, *Biochemistry*, 2009, **48**, 7780–7786.
32 K. G. Sigfridsson, P. Chernev, N. Leidel, A. Popovic-Bijelic, A. Graslund and M. Haumann, *J. Biol. Chem.*, 2013, **288**, 9648–9661.
33 T. M. van der Spek, A. F. Arendsen, R. P. Happe, S. Yun, K. A. Bagley, D. J. Stufkens, W. R. Hagen and S. P. Albracht, *Eur. J. Biochem.*, 1996, **237**, 629–634.
34 Y. Nicolet, A. L. de Lacey, X. Vernede, V. M. Fernandez, E. C. Hatchikian and J. C. Fontecilla-Camps, *J. Am. Chem. Soc.*, 2001, **123**, 1596–1601.
35 J. M. Kuchenreuther, Y. Guo, H. Wang, W. K. Myers, S. J. George, C. A. Boyke, Y. Yoda, E. E. Alp, J. Zhao, R. D. Britt, J. R. Swartz and S. P. Cramer, *Biochemistry*, 2013, **52**, 818–826.
36 A. Silakov, E. J. Reijerse, S. P. Albracht, E. C. Hatchikian and W. Lubitz, *J. Am. Chem. Soc.*, 2007, **129**, 11447–11458.
37 A. Silakov, B. Wenk, E. Reijerse and W. Lubitz, *Phys. Chem. Chem. Phys.*, 2009, **11**, 6592–6599.
38 G. Berggren, A. Adamska, C. Lambertz, T. R. Simmons, J. Esselborn, M. Atta, S. Gambarelli, J. M. Mouesca, E. Reijerse, W. Lubitz, T. Happe, V. Artero and M. Fontecave, *Nature*, 2013, **499**, 66–69.
39 J. Esselborn, C. Lambertz, A. Adamska, T. Simmons, G. Berggren, J. Noth, J. Siebel, A. Hemschemeier, V. Artero, E. Reijerse, M. Fontecave, W. Lubitz and T. Happe, *Nat. Chem. Biol.*, 2013, **9**, 607.
40 A. S. Pereira, P. Tavares, I. Moura, J. J. Moura and B. H. Huynh, *J. Am. Chem. Soc.*, 2001, **123**, 2771–2782.
41 L. Yu, C. Greco, M. Bruschi, U. Ryde, L. De Gioia and M. Reiher, *Inorg. Chem.*, 2011, **50**, 3888–3900.
42 J. W. Tye, M. Y. Darensbourg and M. B. Hall, *Inorg. Chem.*, 2008, **47**, 2380–2388.
43 Z. P. Liu and P. Hu, *J. Am. Chem. Soc.*, 2002, **124**, 5175–5182.
44 P. E. Siegbahn, J. W. Tye and M. B. Hall, *Chem. Rev.*, 2007, **107**, 4414–4435.
45 M. T. Stiebritz and M. Reiher, *Inorg. Chem.*, 2009, **48**, 7127–7140.
46 M. T. Stiebritz and M. Reiher, *Chem. Sci.*, 2012, **3**, 1739–1751.
47 D. W. Mulder, M. W. Ratzloff, E. M. Shepard, A. S. Byer, S. M. Noone, J. W. Peters, J. B. Broderick and P. W. King, *J. Am. Chem. Soc.*, 2013, **135**, 6921–6929.
48 A. R. Finkelmann, M. T. Stiebritz and M. Reiher, *Chem. Sci.*, 2014, **5**, 215, DOI: 10.1039/c3sc51700d.
49 T. B. Rauchfuss, *Science*, 2007, **316**, 553–554.
50 M. Y. Darensbourg and R. D. Bethel, *Nat. Chem.*, 2011, **4**, 11–13.
51 S. Ott, *Science*, 2011, **333**, 1714–1715.
52 F. Gloaguen and T. B. Rauchfuss, *Chem. Soc. Rev.*, 2009, **38**, 100–108.
53 J. M. Camara and T. B. Rauchfuss, *Nat. Chem.*, 2011, **4**, 26–30.
54 B. E. Barton and T. B. Rauchfuss, *Inorg. Chem.*, 2008, **47**, 2261–2263.
55 B. E. Barton and T. B. Rauchfuss, *J. Am. Chem. Soc.*, 2010, **132**, 14877–14885.
56 B. E. Barton, G. Zampella, A. K. Justice, L. De Gioia, T. B. Rauchfuss and S. R. Wilson, *Dalton Trans.*, 2010, **39**, 3011–3019.
57 N. Wang, M. Wang, J. Liu, K. Jin, L. Chen and L. Sun, *Inorg. Chem.*, 2009, **48**, 11551–11558.
58 M. H. Chiang, Y. C. Liu, S. T. Yang and G. H. Lee, *Inorg. Chem.*, 2009, **48**, 7604–7612.
59 B. Jousselme, P. D. Tran, A. Le Goff, J. Heidkamp, N. Guillet, S. Palacin, H. Dau, M. Fontecave and V. Artero, *Angew. Chem., Int. Ed.*, 2011, **50**, 1371–1374.
60 S. E. Smith, J. Y. Yang, D. L. DuBois and R. M. Bullock, *Angew. Chem., Int. Ed.*, 2012, **51**, 3152–3155.
61 P. Glatzel and U. Bergmann, *Coord. Chem. Rev.*, 2005, **249**, 65–95.
62 F. De Groot and A. Kotani, *Core Level Spectroscopy of Solids*, Taylor & Francis CRC Press, Boca Raton, FL, USA, 2008.
63 J. Singh, C. Lamberti and J. A. van Bokhoven, *Chem. Soc. Rev.*, 2010, **39**, 4754–4766.
64 H. Dau, P. Liebisch and M. Haumann, *Anal. Bioanal. Chem.*, 2003, **376**, 562–583.
65 P. A. Lee, P. H. Citrin, P. Eisenberger and B. M. Kincaid, *Rev. Mod. Phys.*, 1981, **53**, 769–806.
66 F. de Groot, *Chem. Rev.*, 2001, **101**, 1779–1808.
67 E. I. Solomon, T. C. Brunold, M. I. Davis, J. N. Kemsley, S.-K. Lee, N. Lehnert, F. Neese, A. J. Skulan, Y.-S. Yang and J. Zhou, *Chem. Rev.*, 2000, **100**, 235–350.
68 X. Wang, C. R. Randall, G. Peng and S. P. Cramer, *Chem. Phys. Lett.*, 1995, **243**, 469–473.
69 X. Wang, M. M. Grush, A. G. Froeschner and S. P. Cramer, *J. Synchrotron Radiat.*, 1997, **4**, 236–242.
70 G. Peng, X. Wang, C. R. Randall, J. A. Moore and S. P. Cramer, *Appl. Phys. Lett.*, 1994, **65**, 2527–2529.
71 P. Glatzel, L. Jacquamet, U. Bergmann, F. M. F. de Groot and S. P. Cramer, *Inorg. Chem.*, 2002, **41**, 3121–3127.
72 N. Leidel, P. Chernev, K. G. Havelius, S. Ezzaher, S. Ott and M. Haumann, *Inorg. Chem.*, 2012, **51**, 4546–4559.

73 N. Leidel, P. Chernev, K. G. Havelius, L. Schwartz, S. Ott and M. Haumann, *J. Am. Chem. Soc.*, 2012, **134**, 14142–14157.
74 N. Leidel, C. H. Hsieh, P. Chernev, K. G. Sigfridsson, M. Y. Darensbourg and M. Haumann, *Dalton Trans.*, 2013, **42**, 7539–7554.
75 K. M. Lancaster, M. Roemelt, P. Ettenhuber, Y. Hu, M. W. Ribbe, F. Neese, U. Bergmann and S. DeBeer, *Science*, 2011, **334**, 974–977.
76 J. Kern, R. Alonso-Mori, R. Tran, J. Hattne, R. J. Gildea, N. Echols, C. Glockner, J. Hellmich, H. Laksmono, R. G. Sierra, B. Lassalle-Kaiser, S. Koroidov, A. Lampe, G. Han, S. Gul, D. Difiore, D. Milathianaki, A. R. Fry, A. Miahnahri, D. W. Schafer, M. Messerschmidt, M. M. Seibert, J. E. Koglin, D. Sokaras, T. C. Weng, J. Sellberg, M. J. Latimer, R. W. Grosse-Kunstleve, P. H. Zwart, W. E. White, P. Glatzel, P. D. Adams, M. J. Bogan, G. J. Williams, S. Boutet, J. Messinger, A. Zouni, N. K. Sauter, V. K. Yachandra, U. Bergmann and J. Yano, *Science*, 2013, **340**, 491–495.
77 G. von Abendroth, S. Stripp, A. Silakov, S. Croux, S. Soucaille, L. Girbal and T. Happe, *Int. J. Hydrogen Energy*, 2008, **33**, 6076–6081.
78 J. M. Kuchenreuther, C. S. Grady-Smith, A. S. Bingham, S. J. George, S. P. Cramer and J. R. Swartz, *PLoS One*, 2010, **5**, e15491.
79 J. Noth, D. Krawietz, A. Hemschemeier and T. Happe, *J. Biol. Chem.*, 2012, **288**, 4368–4377.
80 M. Haumann, P. Liebisch, C. Muller, M. Barra, M. Grabolle and H. Dau, *Science*, 2005, **310**, 1019–1021.
81 H. Dau and M. Haumann, *J. Synchrotron Radiat.*, 2002, **10**, 76–85.
82 S. I. Zabinsky, J. J. Rehr, A. L. Ankudinov, R. C. Albers and M. J. Eller, *Phys. Rev. B: Condens. Matter*, 1995, **52**, 2995–3009.
83 K. V. Klementiev, *freeware*, http://www.cells.es/Beamlines/CLAESS/software/xanda.html.
84 F. Neese, *ORCA: an ab-initio, DFT, and semiempirical electronic structure package. V.2.6.35*, Theoretical Chemistry Group. Max-Planck Institute for Chemical Energy Conversion, Mülheim, Germany, 2009.
85 A. D. Becke, *Phys. Rev. A: At., Mol., Opt. Phys.*, 1988, **38**, 3098.
86 J. P. Perdew, *Phys. Rev. B*, 1986, **33**, 8822.
87 K. Kim and K. D. Jordan, *J. Phys. Chem.*, 1994, **98**, 10089–10094.
88 A. Schäfer, C. Huber and R. Ahlrichs, *J. Chem. Phys.*, 1994, **100**, 5829–5835.
89 S. Sinnecker, A. Rajendran, A. Klamt, M. Diedenhofen and F. Neese, *J. Phys. Chem. A*, 2006, **110**, 2235–2245.
90 A. S. Pandey, T. V. Harris, L. J. Giles, J. W. Peters and R. K. Szilagyi, *J. Am. Chem. Soc.*, 2008, **130**, 4533–4540.
91 L. Noodleman, *J. Chem. Phys.*, 1981, **74**, 5737–5743.
92 F. Neese, *J. Phys. Chem. Solids*, 2004, **65**, 781–785.
93 S. DeBeer-George, T. Petrenko and F. Neese, *J. Phys. Chem. A*, 2008, **112**, 12936–12943.
94 P. Chandrasekaran, S. C. E. Stieber, T. J. Collins, L. Que, F. Neese and S. DeBeer, *Dalton Trans.*, 2011, **40**, 11070–11079.
95 N. Lee, T. Petrenko, U. Bergmann, F. Neese and S. DeBeer, *J. Am. Chem. Soc.*, 2010, **132**, 9715–9727.
96 S. D. DeBeer, M. A. Beckwitz, M. Roemelt, M. N. Collomb, C. DuBoc, T. C. Weng, U. Bergmann, P. Glatzel and F. Neese, *Inorg. Chem.*, 2011, **50**, 8397–8409.
97 I. Zaharieva, P. Chernev, M. Risch, L. Gerencser, G. Berggren, G. Shevchenko, M. Anderlund, T.-C. Weng, M. Haumann and H. Dau, *J. Phys.: Conf. Ser.*, 2009, **190**, 012142–012146.
98 X. Zhao, I. P. Georgakaki, M. L. Miller, J. C. Yarbrough and M. Y. Darensbourg, *J. Am. Chem. Soc.*, 2001, **123**, 9710–9711.
99 S. Löscher, L. Schwartz, M. Stein, S. Ott and M. Haumann, *Inorg. Chem.*, 2007, **46**, 11094–11105.
100 M. Salomone-Stagni, F. Stellato, C. M. Whaley, S. Vogt, S. Morante, S. Shima, T. B. Rauchfuss and W. Meyer-Klaucke, *Dalton Trans.*, 2010, **39**, 3057–3064.
101 T. Happe and J. D. Naber, *Eur. J. Biochem.*, 1993, **214**, 475–481.
102 G. Goldet, C. Brandmayr, S. T. Stripp, T. Happe, C. Cavazza, J. C. Fontecilla-Camps and F. A. Armstrong, *J. Am. Chem. Soc.*, 2009, **131**, 14979–14989.
103 M. Bruschi, C. Greco, P. Fantucci and L. De Gioia, *Inorg. Chem.*, 2008, **47**, 6056–6071.
104 U. Ryde, C. Greco and L. De Gioia, *J. Am. Chem. Soc.*, 2010, **132**, 4512–4513.
105 D. E. Schwab, C. Tard, E. Brecht, J. W. Peters, C. J. Pickett and R. K. Szilagyi, *Chem. Commun.*, 2006, 3696–3698.
106 T. R. Simmons and V. Artero, *Angew. Chem., Int. Ed.*, 2013, **52**, 6143–6145.
107 P. Glatzel, U. Bergmann, F. M. F. de Groot and S. P. Cramer, *Phys. Rev. B: Condens. Matter*, 2001, **64**.
108 S. Bonhommeau, N. Pontius, S. Cobo, L. Salmon, F. M. de Groot, G. Molnar, A. Bousseksou, H. A. Durr and W. Eberhardt, *Phys. Chem. Chem. Phys.*, 2008, **10**, 5882–5889.
109 P. Knörzer, A. Silakov, C. E. Foster, F. A. Armstrong, W. Lubitz and T. Happe, *J. Biol. Chem.*, 2011, **287**, 1489–1499.
110 M. Winkler, J. Esselborn and T. Happe, *Biochim. Biophys. Acta, Bioenerg.*, 2013, **1827**, 974–985.
111 A. J. Cornish, K. Gartner, H. Yang, J. W. Peters and E. L. Hegg, *J. Biol. Chem.*, 2011, **286**, 38341–38347.
112 T. Lautier, P. Ezanno, C. Baffert, V. Fourmond, L. Cournac, J. C. Fontecilla-Camps, P. Soucaille, P. Bertrand, I. Meynial-Salles and C. Leger, *Faraday Discuss.*, 2011, **148**, 385–407.
113 K. A. Vincent, A. Parkin, O. Lenz, S. P. Albracht, J. C. Fontecilla-Camps, R. Cammack, B. Friedrich and F. A. Armstrong, *J. Am. Chem. Soc.*, 2005, **127**, 18179–18189.
114 A. Parkin, C. Cavazza, J. C. Fontecilla-Camps and F. A. Armstrong, *J. Am. Chem. Soc.*, 2006, **128**, 16808–16815.
115 M. Winkler, S. Kuhlgert, M. Hippler and T. Happe, *J. Biol. Chem.*, 2009, **284**, 36620–36627.

116 S. Morra, F. Valetti, S. J. Sadeghi, P. W. King, T. Meyer and G. Gilardi, *Chem. Commun.*, 2011, **47**, 10566–10568.
117 H. Krassen, S. Stripp, G. von Abendroth, K. Ataka, T. Happe and J. Heberle, *J. Biotechnol.*, 2009, **142**, 3–9.
118 F. A. Armstrong, *Photosynth. Res.*, 2009, **102**, 541–550.
119 C. Baffert, L. Bertini, T. Lautier, C. Greco, K. Sybirna, P. Ezanno, E. Etienne, P. Soucaille, P. Bertrand, H. Bottin, I. Meynial-Salles, L. De Gioia and C. Leger, *J. Am. Chem. Soc.*, 2011, **133**, 2096–2099.
120 C. E. Foster, T. Kramer, A. F. Wait, A. Parkin, D. P. Jennings, T. Happe, J. E. McGrady and F. A. Armstrong, *J. Am. Chem. Soc.*, 2012, **134**, 7553–7557.
121 A. F. Wait, C. Brandmayr, S. T. Stripp, C. Cavazza, J. C. Fontecilla-Camps, T. Happe and F. A. Armstrong, *J. Am. Chem. Soc.*, 2011, **133**, 1282–1285.